Characterizing the Movement of Contaminant Liquid Metal Particles when Subject to Electric Pulses, Within the Context of Z-pinch Fusion Reactors

Vignesh Sridhar

Thesis submitted to the Faculty of the

Virginia Polytechnic Institute and State University

in partial fulfillment of the requirements for the degree of

Master of Science

in

Aerospace Engineering

Colin S. Adams, Chair

Stefano Brizzolara, Co-chair

Luca Massa

August 13, 2024

Blacksburg, Virginia

Keywords: Image Processing, Magneto-hydrodynamics, Liquid Metals, Z-pinch Fusion

Copyright 2024, Vignesh Sridhar

Characterizing the Movement of Contaminant Liquid Metal Particles when Subject to Electric Pulses, Within the Context of Z-pinch Fusion Reactors

Vignesh Sridhar

(ABSTRACT)

This thesis examines the behavior of contaminant liquid metal particles, known as ejecta, which are expelled from magnetically-accelerated liquid metal surfaces, in Z-pinch fusion reactors. These ejecta present significant contamination risks to plasma fuel in fusion reactors. The study employed a liquid electrode setup, exposing a eutectic tin-bismuth mixture to high-current pulses. Particle motion was tracked and analyzed using high-speed camera footage processed with advanced techniques, including contrast limited adaptive histogram equalization (CLAHE), neutral-density filtering, and Sobel edge detection. The research integrates automated particle tracking algorithms with connected-component labeling and two-point correlation functions to monitor ejecta trajectories. Results reveal an average ejected particle velocity of 2.54 m/s ($\pm$3.58 m/s), with particle formation likelihood peaking at velocities around 1.14 m/s. These findings indicate that particle ejection dynamics are influenced by factors such as initial temperature, vacuum conditions, and electrostatic forces. This research provides crucial insights for optimizing reactor design and mitigating contamination in future fusion energy applications. The study also proposes directions for further investigation, including the temperature dependency of particle ejection dynamics and the implementation of improved heating systems for experimental setups.

Characterizing the Movement of Contaminant Liquid Metal Particles when Subject to Electric Pulses, Within the Context of Z-pinch Fusion Reactors

Vignesh Sridhar

(GENERAL AUDIENCE ABSTRACT)

This thesis explores how tiny particles of liquid metal, called ejecta, behave when exposed to powerful electric pulses in a type of nuclear fusion reactor known as a Z-pinch reactor. These particles, which are thrown out from the surface of liquid metal during fusion experiments, can contaminate the fuel and reduce the efficiency of the fusion reactor. The study involves a series of experiments where a special mixture of metals, tin and bismuth, is subjected to high electrical currents. Using advanced image processing techniques, such as digital enhancement and edge detection, the movement of these particles was tracked with high-speed cameras. The findings reveal that the average speed of these particles is about 2.54 meters per second, and their formation is most likely at speeds around 1.14 meters per second. The results suggest that factors like temperature, vacuum conditions, and electromagnetic forces significantly affect how these particles are ejected. Understanding this behavior is important for improving the design and performance of future fusion reactors, which aim to provide a clean and almost limitless source of energy. The study also points to further research opportunities, including examining how different temperatures affect the behavior of these particles and enhancing the experimental setup to better control heating conditions.

Dedication

To my parents, Anitha and Sridhar, and my grandmother, Girija.

Acknowledgments

I could not have completed this work without the unyielding support of my parents, who have stood by and supported me through my many ups and downs. Thank you for always believing in me, and especially during times when I found it difficult to do so myself. My friends, both in Blacksburg and elsewhere, have been instrumental to my progress. Thank you for bearing with me as I clumsily made my way through graduate school, for always being there for me and ensuring that I never once felt alone. You all are the best, and I am excited for a lifetime of adventures with you. I am deeply grateful to all my lab mates at the Experimental Plasma and Propulsion Laboratory for their support throughout my research. Dan was an exceptionally patient teacher as I learned the intricacies of our work. From my first day in the lab to the morning of my thesis defense, Dan guided me not only through the scientific and engineering challenges but also helped me grow as an engineer and a person. Trent and Ameer were also wonderful mentors who were always open to help when needed. My advisor, Dr Adams, gave me the opportunity to join the lab and work on interesting topics. He was always helpful and insightful, and his knowledge proved invaluable as this research progressed. I am grateful for our conversations which always improved my grasp of a problem and refined my understanding of how to be a researcher. I'd also like to thank Dr Brizzolara and Dr Massa for always making time for me and helping me through this thesis.

Contents

List of Figures **viii**

1 Introduction **1**

1.1 Nuclear Fusion Background 2

1.2 Liquid Metals Background 9

1.3 Potential Impact of Work 11

2 Experiment Design **12**

3 Particle tracking efforts to ascertain core contamination **18**

3.1 Experiment Description 18

3.2 Ejected Droplets 21

3.3 Theory of Algorithms Utilized 23

3.4 Image Processing 24

3.5 Calculation of Ejecta Positions 33

3.6 Results 49

3.7 Comparison with Manual Tracking 55

4 Liquid Electrode Experiment Upgrade **59**

4.1 Choosing a new heater and assembly 60

5 Summary **63**

6 Future Works **65**

6.1 Heat Dependency of the System 65

Bibliography **66**

Appendix A MATLAB Codes **76**

List of Figures

1.1 This diagram shows a Z-pinch configuration, where an axial electric current (labeled "E" and shown by the black arrows) flows through a plasma column, generating an azimuthal magnetic field (denoted "B" and illustrated with curved arrows). The magnetic field circles around the plasma due to the current. The blue "+" symbol represents positively charged ions while the pink "-" symbol represents electrons moving in the opposite direction. The inward magnetic pressure, produced by the interaction between the current and the azimuthal magnetic field, compresses the plasma. 5

1.2 ZaP Experiment diagram. In this configuration, gas is pushed from the left. The plasma is accelerated through the neutral gas injection plane, and the assembly region is where the z-pinch occurs. The system is designed to study the stabilization of the z-pinch over time[7]. 8

2.1 The figure shows the pulse forming network used in this experiment, comprised of capacitors, buswork, switches, and transmission lines. The blue and gray units are the capacitors, which store and discharge energy in controlled pulses. The wooden platform below the setup ensures stability and insulation. Wires and switches connect the capacitors to the rest of the system, facilitating the transmission of high-voltage pulses used for testing. The white covering across the top provides electrical insulation. 13

2.2 3-D rendering of chamber holding liquid metal. 14

2.3 Photron FastCam Mini AX 200. The camera (black and red) is placed within a Faraday cage (gray), an enclosure used to block electromagnetic fields. This shielding aims to promote data collection by the high-speed camera. 15

2.4 Side-view of chamber, as part of the experimental setup. The camera would ordinarily be placed in the Faraday cage on the right, and the viewport in the center is used as a place to allow light to enter the chamber on trigger. The insulated cylinder on the left is the reservoir where the metal is stored in its solid state when not being used in a trial. 16

3.1 Path that current takes entering and leaving the chamber the current enters through the wire, moves down to the base of the chamber, and out via the walls and to ground. 19

3.2 Region around wire as seen in the liquid metal chamber which is used as an area of interest in particle tracking efforts. 20

3.3 The particles circled in red are the ejecta particles that need to be tracked. As noticed, there is very little, and varying, contrast with the background. Only the particles within the region around the wire are tracked as the background makes the ejecta particles 'pop' out when the images are properly processed. 21

3.4 Edge tracking method applied on a test dated June 24th, 2022. The green markers are populated around particles that have enough of a difference in intensity with the surrounding pixels. The green markers are used instead of lines as the density of markers is used in later steps to calculate the centroid (shown in red). 24

3.5 Image resizing for better view for a test performed on June 24th, 2022, utilizing the tenth image shot. The image on the left is the raw image data captured by the camera, and the image on the right shows the region of interest used in this study. Thus region is highlighted in the red oval within the image on the left. 25

3.6 Histograms associated with initial denoising of images using CLAHE Algorithm, the 'smoothing' effect on the pixel intensities is clearly depicted. . . . 26

3.7 CDF of image before and after CLAHE algorithm is applied. The top plot shows pixel intensities which are concentrated in a narrow range, resulting in poor contrast. The bottom plot shows that the algorithm redistributes pixel intensities more evenly by applying localized contrast adjustments and limiting histogram amplification to prevent noise amplification. 27

3.8 CLAHE enhanced image (left) and N-D filtered image (right). The image on the right demonstrates the effect of a N-D filter, which reduces image brightness and smooths intensity variations without enhancing local details, resulting in a blurred appearance with reduced contrast and definition. . . . 29

3.9 The image on the left displays the result of applying a Mean Filter for subtraction, which smooths the image by averaging pixel values over a uniform window, leading to less localized smoothing and more block-like artifacts. The Gaussian filtered image on the right uses Gaussian-weighted kernel, resulting in more natural blurring and a gradual transition between pixel intensities. While the Gaussian Filter typically preserves finer details, the Mean Filter can be advantageous when the primary goal is to reduce high-frequency noise uniformly across an image, leading to a more generalized smoothing effect). . 30

3.10 Subtracted figure, binarized. As seen, the variations of the light intensities are more easily observed. This is a crucial step in setting up the images that later aids in the calculations of the ejecta positions. In this image, the white regions are more likely ejecta particles, which will be confirmed in subsequent steps. 31

3.11 Noise variation across frames, logarithmic scale. The red curve, which shows the noise variance after filtering, is substantially lower, demonstrating the effectiveness of the median filter in reducing high-frequency noise while preserving critical image details such as edges. 32

3.12 Subtracted image using mean filter (right), and binarized image put through the median filter (left). 33

3.13 Selection of Region of Interest for calculations. This is the region within which most ejecta are observed over a significant number of frames. 34

3.14 Input images for blend operations using linear interpolation. 36

3.15 The image on the left represents the result of blending two input images using linear interpolation. The blending factor ($\alpha = 0.5$) ensures that both input images contribute equally to the output, allowing the visibility of intensity variations in both regions. The purple and green colors are used to show the regions which are clearly at different intensity levels than their immediate surroundings. The image on the right is the corresponding grayscale version of the blended output. 36

3.16 Comparison of pixel intensities before and after processing methods are applied. The processed image (on the bottom) shows a more evenly distributed range of pixel intensities that indicates improved separation between background noise and potential ejecta regions. This distinction in intensity levels is beneficial for classifying ejecta particles. 38

3.17 Sobel filters for edge detection in the x and y directions 39

3.18 Gradients calculated using Sobel kernels for edge detection, shown on the right. 41

3.19 Gradient calculation directions of the processed image. The darker colors (indicated on the larger numbers in the color bar) correspond to stronger edges, which indicate potential ejecta particles. 42

3.20 Results, after Sobel method of edge detection is applied. 43

3.21 Visual representation, when edge components are connected using 8-connectivity connected-component labeling. Previously calculated edge pixels were connected in order to depict the edge of each ejecta particle as a whole. 45

3.22 Edges and centroid, calculated for the 60th frame of an experimental run on June 24th, 2022. 47

3.23 Area sizes of tracked edges, across all frames. 48

3.24 This graph shows the 2-point correlation of the centroid distances. It showcases the centroids which are most frequently observed by the code. 2-point correlation finds the probability of finding two points within a certain distance of each other. 51

3.25 Tracked particles, in the sixth frame for June 24th 2022. 54

3.26 This plot shows the trajectories of particles that were tracked across all of the frames of this analysis. 55

3.27 These plots show the likelihood that an ejecta particle will form, studied at different velocities based on the mass of each particle. The plot on the left is the result of manual tracking efforts, while the one on the right is derived from the automatic tracking efforts detailed in this Thesis. The manual tracking identified the highest likelihood of ejecta formation at 3.47 m/s, while the automatic tracking identified at 1.14 m/s. 57

4.1 The image shows the PID (Proportional-Integral-Derivative) controller used to regulate the temperature in both the chamber and the reservoir during the experiment. The controller adjusts the output of the heaters based on feedback from two thermocouples placed in the chamber and reservoir. . . . 60

4.2 This image shows the Chromalox A-65 heater selected for the experiment upgrade. The ring design ensures uniform heat distribution across the chamber. 61

4.3 This image shows the bottom of the chamber after the installation of the new Chromalox A-65 ring heater. The wires shown are soldered to the bottom of the heater, which are connected to the PID control system. 62

Chapter 1

Introduction

Nuclear fusion is potentially one of the most sustainable sources of high-power, clean energy. Endeavors to achieve break-even fusion have accelerated in the recent past. This body of work aims to add to a small subset of these efforts. Plasma-facing components (PFCs) in fusion reactors have a high risk of erosion. A promising method to combat this is through the use of liquid metals as a self healing PFC layer on top of solid substrate. This research focuses on implementation of this method within z-pinch fusion reactors.

Nuclear fission is widely used commercially today. This process is a reaction which splits nuclei apart, releasing energy in the process. Most fission power plants in the United States split uranium-235 [1]. Fusion, on the other hand, is a process wherein two lighter nuclei merge to form a nucleus that is heavier than each of the smaller nuclei. However, the products of this reaction are less massive than the reacting nuclei. The 'leftover' mass is released as energy [2]. The fuel used in fusion reactions may be in the form of plasma. Fusion reactors heat plasma to temperatures of over 100 million degrees Celsius using magnetic fields (the z-pinch concept is examined here) or high-powered lasers confine the plasma for sufficient time that fusion reactions produce more energy than required to assemble the fuel [59].

In this research effort, a wire is employed as a surrogate for a plasma column. This wire delivers large electric current pulses which come into contact with the liquid metal. This liquid metal is held within a heated chamber for testing in liquid form, but is solid at room temperature. The phenomena that occur when the liquid metal is exposed to these large

current pulses all happen within a few milliseconds. The phenomena are observed through a high-speed camera. The main objective in this research is to characterize the velocity of some of the liquid metal particles that pose a potential contamination risk in the fuel. These particles have different trajectories when compared to the larger pool of liquid metal in the chamber. Liquid metal - electric current interactions are analyzed within the context of their behaviors in a Z-pinch concept fusion reactor (discussed in the next section).

1.1 Nuclear Fusion Background

The most commonly proposed fusion reaction for energy production is the deuterium-tritium (D-T) reaction. Both are isotopes of hydrogen. Deuterium has an atomic mass of 2.014 atomic mass units (AMU), while tritium has an atomic mass of 3.016 AMU. In a reaction, this is 5.030 AMU of D-T being fused, which provides 4.0026 AMU of helium, a neutron of 1.009 AMU is ejected, and 14.1 MeV of energy is released [2]. Equation 1.1 shows that this energy is due to the mass difference of 0.02 AMU between the products and the reactants [6].

$$ {}^{2}_{1}\mathrm{D}^{+} + {}^{3}_{1}\mathrm{T}^{+} \rightarrow {}^{4}_{2}\mathrm{He}^{++} + {}^{1}_{0}\mathrm{n} \tag{1.1} $$

This D-T reaction is interesting for a few reasons, notably including the abundance of fuel. Deuterium is considered naturally abundant, as it accounts for 0.0312% of all hydrogen in the oceans. Tritium, meanwhile, can be bred from lithium during the fusion reaction itself as the resulting neutrons interact with lithium, showing in equations 1.2 and 1.3. Neutron bombardment of lithium-6 or lithium-7 can produce tritium via the following reactions [60]:

$$^{6}\mathrm{Li} + \mathrm{n} \rightarrow \mathrm{T} + \alpha \tag{1.2}$$

$$^{7}\mathrm{Li} + \mathrm{n} \rightarrow \mathrm{T} + \alpha + \mathrm{n} \tag{1.3}$$

This is an important reason why the usage of liquid metals in fusion reactors is investigated, and will be discussed in the subsequent sections. Currently, lithium reserves in the Earth's crust can last us 250-600 years of fusion energy [3]. However, lithium can also be extracted from seawater, which leads to an 'unlimited' (a few million years' worth) supply of both deuterium and tritium [61]. Reportedly, concentrations of lithium vary from 170 to 190 μg/L in seawater [62]. It should be noted that the British diplomat Claude MacDonald once declared ninety-nine years to be 'as good as forever' in reference to his nation's lease of Hong Kong, suggesting that there was ample time to worry about Hong Kong's return to China. However, we might have slightly longer than Mr. MacDonald to solve the fuel supply challenges posed by fusion energy [63].

Apart from the abundance of fuel, developing fusion energy also comes with a whole host of advantages. These include a significant decrease in safety concerns due to the high temperatures at which these reactions occur and the small amounts of input materials used, both of which lead to a reduced potential for harmful runaway reactions when compared to fission processes [64].

Currently, fusion reactors consume more energy than they produce, with a major challenge being the endurance of plasma-facing materials while preventing contamination of plasma by wall materials. The Liquid Electrode eXperiment (LEX) at Virginia Tech addresses these challenges by studying the dynamic behavior of liquid electrodes under current densities

relevant to z-pinch fusion reactors.

Z-pinch fusion is a theoretically simple form of magnetic confinement of plasmas. The concept of magnetic confinement employs the use of a magnetic field to confine the movement of plasma [8]. A steady magnetic field does not directly change the magnitude of the velocity of a charged particle (such as plasma). Instead, it affects only the direction of the particle's velocity, causing the particle to follow a curved path (like a circular or spiral motion). This phenomenon is due to the Lorentz force, which acts perpendicular to both the magnetic field and the particle's velocity. As a result, the steady magnetic field changes the particle's direction without affecting its speed (magnitude of velocity), assuming no other forces are acting on it [9]. The z-pinch idea is one that involves a current flowing through a plasma column. The self-generated magnetic field acts as a counterbalance to the radial plasma pressure that acts outward. The magnetic field acts inward and 'pinches' the plasma into compression. The diagram below shows a z-pinch configuration.

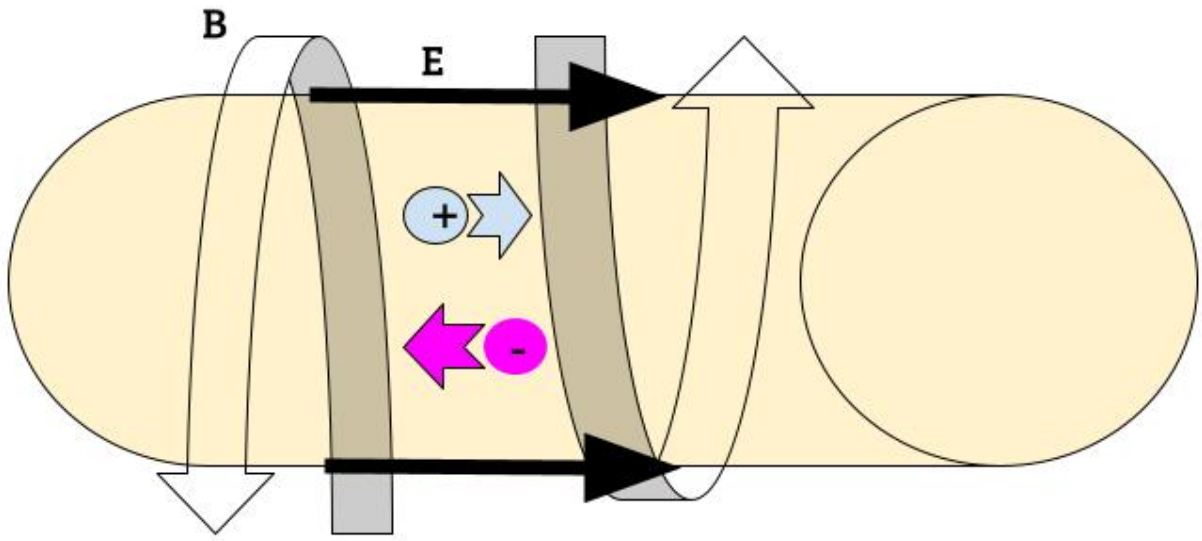

Figure 1.1: This diagram shows a Z-pinch configuration, where an axial electric current (labeled "E" and shown by the black arrows) flows through a plasma column, generating an azimuthal magnetic field (denoted "B" and illustrated with curved arrows). The magnetic field circles around the plasma due to the current. The blue "+" symbol represents positively charged ions while the pink "-" symbol represents electrons moving in the opposite direction. The inward magnetic pressure, produced by the interaction between the current and the azimuthal magnetic field, compresses the plasma.

A Z-pinch can be produced through various methods, including gas injection [72], wire arrays [73], or linear-driven configurations [74], each relying on the rapid compression of plasma by strong electromagnetic forces. In a typical gas-puff Z-pinch, neutral gas, such as deuterium or tritium, is injected into a central chamber and then ionized by a high-voltage pulse, forming a conductive plasma column. A powerful pulsed electrical current is then driven through the plasma, creating an intense azimuthal magnetic field that compresses the plasma towards the axis, increasing its temperature and density to conditions suitable for nuclear fusion [65].

In proposed energy-producing Z-pinch reactors, this process must be rapidly repeated to sustain energy production. The cycle begins with the injection and ionization of fresh gas, followed by the compression phase, where the plasma is pinched to achieve high densities and temperatures. After reaching the peak compression (stagnation) state, the plasma begins

to expand outward. The reactor then clears the chamber of residual plasma and impurities, prepares the chamber environment for the next pulse, and re-injects gas, aiming for minimal delay between pulses to maximize energy output [66].

Efficient control of the electromagnetic forces during each pinch event is essential for maintaining plasma confinement, optimizing plasma conditions, and mitigating the intense thermal and neutron loads produced. Stability in the plasma depends on carefully managing these forces and plasma conditions. The precise synchronization of these processes, along with advanced materials for reactor walls and rapid cooling systems, are key factors in achieving the desired fusion power output and reactor longevity.

The z-pinch configuration is susceptible to instabilities, which has been an impediment to usage as a fusion source. The perturbations form local fluctuations in the magnetic field, which leads to $m = 0$ and $m = 1$ ('sausage' and 'kink') modes, which rapidly deteriorates the confinement of plasma [10]. Liquid metals can absorb and dissipate the intense heat and particle fluxes generated by the plasma, reducing wall erosion and maintaining structural integrity. Additionally, the self-healing properties of liquid metal walls and their ability to absorb impurities contribute to maintaining plasma integrity. While these features improve confinement by reducing contamination, they do not directly counter the 'sausage' ($m = 0$) or 'kink' ($m = 1$) modes of instability, which are more closely related to magnetic forces and plasma current distribution [67].

The *Kruskal-Shafranov condition* provides a stability criterion for plasmas confined in a toroidal geometry within the magnetohydrodynamic (MHD) framework, ensuring that the ratio of the toroidal magnetic field (B_T) to the poloidal magnetic field (B_θ) is sufficient to prevent certain types of instabilities. The condition is mathematically expressed as

$$q(a) = \frac{B_T a}{B_\theta R} > 1,$$

where $q(a)$ is the safety factor, a is the minor radius of the torus, and R is the major radius. In this context, the safety factor q represents the number of times a magnetic field line wraps around the torus toroidally for each poloidal loop.

However, this criterion applies specifically to toroidal confinement devices, such as tokamaks, where both toroidal and poloidal magnetic fields exist. In a Z-pinch configuration, which lacks an axial (toroidal) magnetic field and has no major radius, the safety factor q would be undefined. Alternative stabilizing mechanisms, such as using close-fitting conductors around the plasma, are explored to address stability concerns in Z-pinches. However, while liquid metal coatings may help with heat management and impurity absorption, they do not directly contribute to stabilization. A wall positioned close enough to impact plasma stability would be infeasible in a Z-pinch reactor due to the extreme proximity required, whether the material is liquid or solid. [68].

Figure 1.2 depicts the ZaP Flow Z-pinch experiment that was performed at the University of Washington [7].

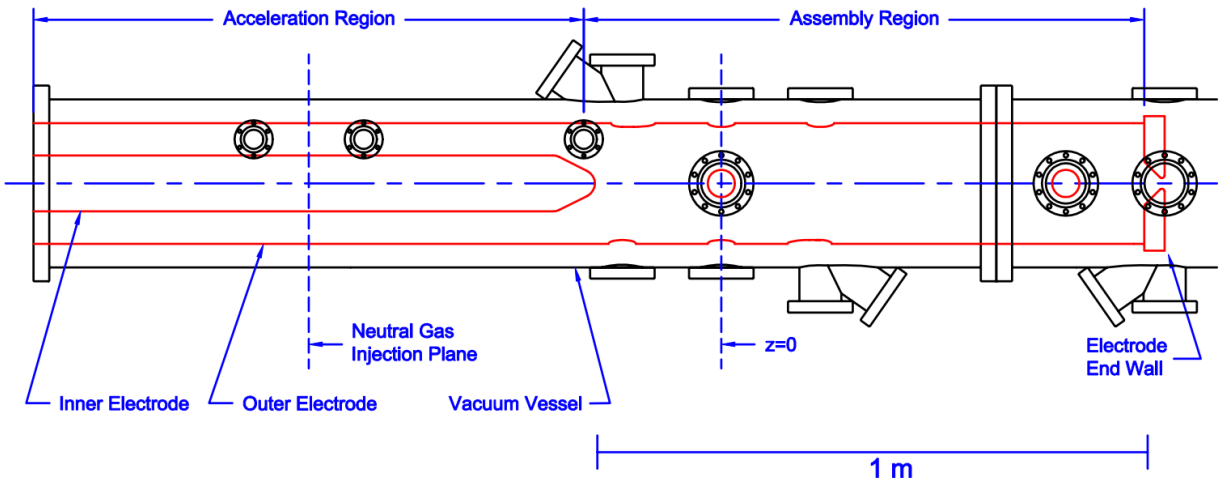

Figure 1.2: ZaP Experiment diagram. In this configuration, gas is pushed from the left. The plasma is accelerated through the neutral gas injection plane, and the assembly region is where the z-pinch occurs. The system is designed to study the stabilization of the z-pinch over time[7].

In this configuration, a flowing liquid metal layer would be used at the 'electrode end wall' section. This configuration is designed to study the stabilization mechanisms of the Z-pinch by utilizing sheared axial plasma flows to mitigate instabilities such as the sausage and kink modes. The inner electrode provides a path for the current that generates a magnetic field, which induces the plasma to compress via the Lorentz force. The outer electrode helps to contain the plasma, while the vacuum vessel maintains the required low-pressure environment. The ZaP experiment aims to demonstrate longer plasma confinement times and higher densities, which are critical for advancing the feasibility of Z-pinch fusion as a compact and efficient energy source [69] [70].

1.2 Liquid Metals Background

Liquid metals as plasma facing components within fusion reactors is not a new idea, and has been under consideration since the 1950s. In 1979, Badger et al. [12] discussed a design for a toroidal fusion reactor at the University of Wisconsin. This paper also laid out potential uses for liquid metals in fusion reactors. Among the advantages they outlined was the ability of liquid metals to reduce the irradiation of structural components, specifically by acting as a barrier to the high-energy neutrons produced in the fusion process. Since then, other studies have investigated the advantages of using liquid metals in fusion reactors. The research in this thesis focuses on three of these advantages:

1. liquid metals can limit damage due to erosion within the chamber,
2. liquid metals are suitable for heat transfer, which are crucial to managing the high thermal loads within the fusion reactor,
3. if lithium is used as one of the constituents in the alloy, tritium fuel can be bred to supply the reactor in the future.

All three of these points are important as they increase commercial efficiency and make nuclear fusion a more viable target. The third item in the list is particularly crucial to the overarching goal of making fusion a self-sustaining energy source. Self-breeding will enable this long-term operation. The most stable isotopes of lithium are lithium-6 and lithium-7. The following fission reactions are the most common involving interactions between lithium and a neutron. All produce tritium, as shown, and also an alpha particle which is akin to ^{4}He [13]:

$$^6\mathrm{Li} + n \rightarrow \alpha + \mathrm{T} + 4.78 \text{ MeV} \quad (E_{th} = 2.47 \text{ MeV, threshold energy}) \tag{1.4}$$

$$^{7}\mathrm{Li} + n \rightarrow \alpha + \mathrm{T} + n \tag{1.5}$$

$$^{7}\mathrm{Li} + n \rightarrow 2\mathrm{T} + 2n' \tag{1.6}$$

While the goal is to use lithium as a consituent of the liquid metal, a eutectic mix of tin and bismuth (SnBi) was used in the research presented in this thesis. A eutectic mix is a homogeneous mixture that has a melting point that is lower than that of its constituents [14]. Tin has a melting point of 505 K, while bismuth has a melting point of 544 K [15] [16]. The physical properties of tin and bismuth are suitable for the experiments that are analyzed in this thesis, particularly low melting point, low vapor pressure, and low relative magnetic permeability. This research uses a 58% bismuth, and 42% tin mixture, which results in a melting point of 411 K [17]. The mass density of this mixture is $8.603 \times 10^{3}\,\mathrm{kg/m^{3}}$, and its viscosity is $2.825 \times 10^{-3}\,\mathrm{Pa \cdot s}$ at 423 K. These values are important for the estimation of the mass of the ejected particles.

These liquid metals also hold significant promise in broader applications. Beyond their potential contribution to fusion technology for energy production, they offer possibilities in aerospace applications, particularly in space propulsion. A shielding effect comes from the high density of low-Z (low atomic number) nuclei, which help scatter and slow down neutrons. Hydrogen nuclei, with their lower atomic number, are even more effective in providing neutron shielding in space environments, protecting electronic systems and astronauts from the harmful high-energy neutrons in deuterium-tritium fusion reactions [71]. The fusion reaction in the propulsion system would theoretically release a significant amount of energy, which would heat the propellant and convert it into high-velocity plasma. This process increases the exhaust velocity and thrust of the rocket. Additionally, in proposed fusion propulsion systems, energetic neutrons generated from reactions can interact with materials like lithium, potentially leading to secondary reactions. Although secondary fusion reactions

may produce additional particles, these particles are not directed and therefore have a negligible effect on the device's overall thrust. The primary mechanism for increased propulsion efficiency comes from the high energy released in the fusion reaction itself, which drives the exhaust velocity, rather than a substantial increase in mass flow [5].

1.3 Potential Impact of Work

In the context of the Liquid Electrode eXperiment at Virginia Tech, ejecta refer to small particles of liquid metal that are expelled from the pool of liquid when exposed to a current. These introduce impurities into plasma in a repetitively pulsed fusion reactor, compromising the purity of the fuel, which in turn reduces the likelihood of plasma-plasma reactions. Understanding and mitigating the impact of ejecta is crucial for enhancing the performance and longevity of future z-pinch fusion reactors. Detecting and tracking these ejecta particles provides a foundation for developing strategies to minimize contamination, thereby optimizing plasma performance.

Identifying the conditions that lead to increased ejecta production, this research informs the design of reactor components and operational protocols that mitigate these effects. Such insights could be the key to achieve long-term sustainability and cost-effectiveness in fusion energy production. This work focuses on developing an image processing sequence that can detect these particles in the absence of stable illumination. These techniques can be used in various other fields for similar applications.

Chapter 2

Experiment Design

The Liquid Electrode eXperiment at Virginia Tech was constructed to observe how liquefied metal reacts when exposed to pulsed currents, and as a result, magnetic fields. The electricity flow simulates a column of plasma that would interact with the liquid metal in a z-pinch fusion reactor. The inclusion of liquid metal in such a reactor could increase fuel efficiency due to tritium breeding, and increase the life-span of fusion reactors when a self-sustaining D-T reaction is realized.

The setup was designed in order to deliver a current to a pool of liquid metal. There are eight capacitors that make up a pulse forming network. A custom power feed-through pushes the current through a network of wires, through target wires of varying radii (depending on test objectives) in the range of 1.59 - 2.38 mm. Figure 2.1 shows the pulse forming network.

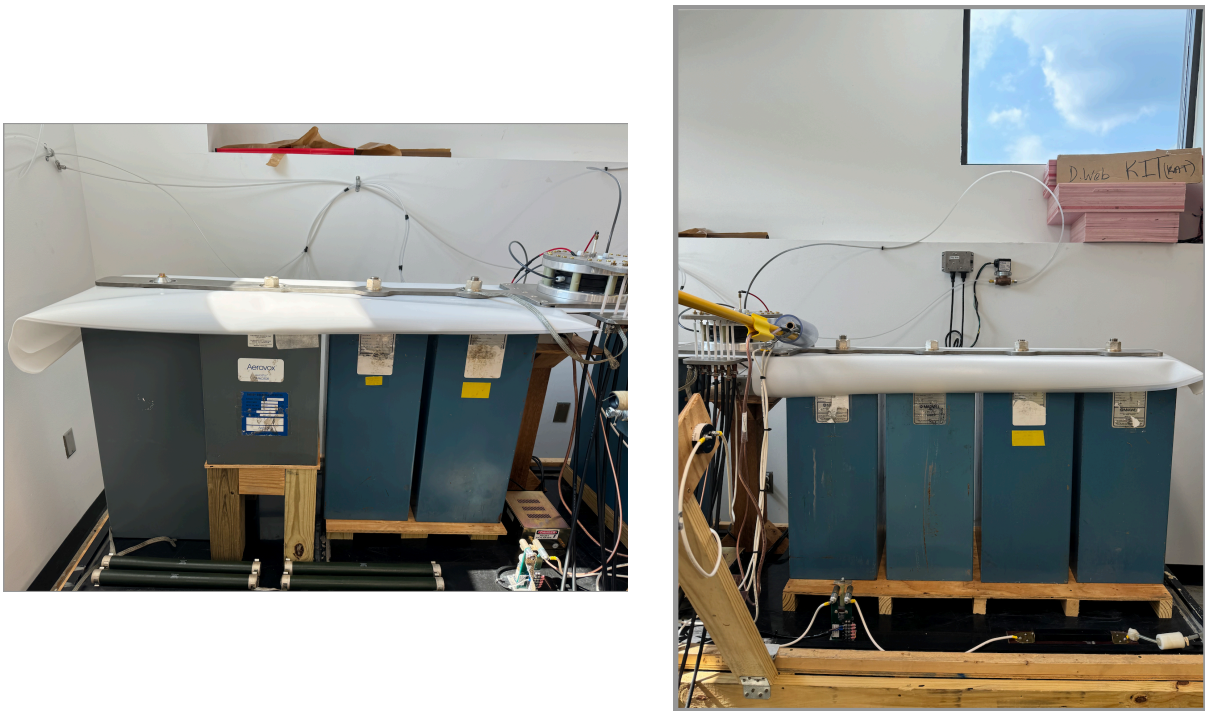

Figure 2.1: The figure shows the pulse forming network used in this experiment, comprised of capacitors, buswork, switches, and transmission lines. The blue and gray units are the capacitors, which store and discharge energy in controlled pulses. The wooden platform below the setup ensures stability and insulation. Wires and switches connect the capacitors to the rest of the system, facilitating the transmission of high-voltage pulses used for testing. The white covering across the top provides electrical insulation.

Figure 2.1 shows the two legs of the capacitor bank. One of the legs has four capacitors of 6 µF, and the other leg has two capacitors of 100 µF each, and two of 6 µF. The system in total is capable of applied potentials up to 20 kV, and is capable of delivering current pulses of up to 250 kA. For the tests used in this work, the potentials were in the range of 5-7 kV, and the PFN delivered current pulses of around 100 kA.

Figure 2.2: 3-D rendering of chamber holding liquid metal.

Figure 2.2 shows a 3-D rendering of the chamber, courtesy of Dr. Daniel Weber. The eutectic mix of tin and bismuth is solid at room temperature. This solid metal sits in a reservoir, which is connected to the chamber, where the melted liquid metal is transferred to for experimental runs. Both have their own heater systems in order to melt the liquid metal, and also keep the state of the metal liquid throughout the experiment. For this project, the reservoir and chamber were heated to 443.15 K.

The heating capabilities were upgraded over the course of the author's research efforts (discussed in a later chapter). There are two data recording mechanisms in place. The first is a high-speed camera (a Photron FastCam Mini AX 200), and is more relevant to this document. The second is a Rogowski coil that measures the current [42]. The high-speed camera is rated for a maximum frame rate of 900,000 [46] frames per second. Ordinarily, this study is run at 20,000–30,000 frames per second. This is used in calculations for velocity of 'ejecta' particles later in the document. Two lenses, a 50 mm and 130 mm, were used

in data collection. The 50 mm lens was predominantly used in this study as it was able to capture larger motion of the liquid metal, with most of the LM free surface within the field of view. Figure 2.3 shows the high-speed camera, mounted on the experiment.

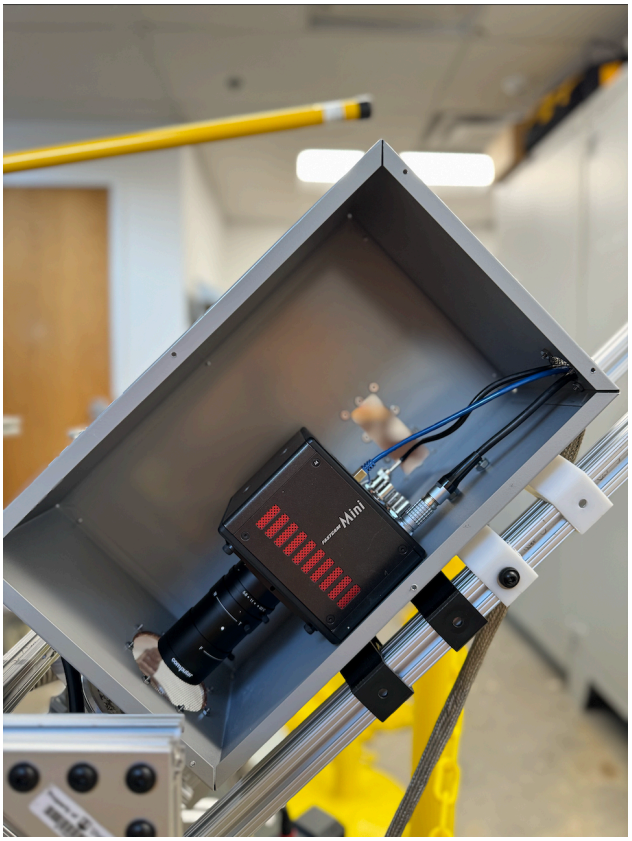

Figure 2.3: Photron FastCam Mini AX 200. The camera (black and red) is placed within a Faraday cage (gray), an enclosure used to block electromagnetic fields. This shielding aims to promote data collection by the high-speed camera.

Figure 2.4 shows the side-view of the rest of the experimental setup, depicting the arrangement of key components such as the chamber (center), Faraday cage (open box to the right), and viewport (circular feature in the front).

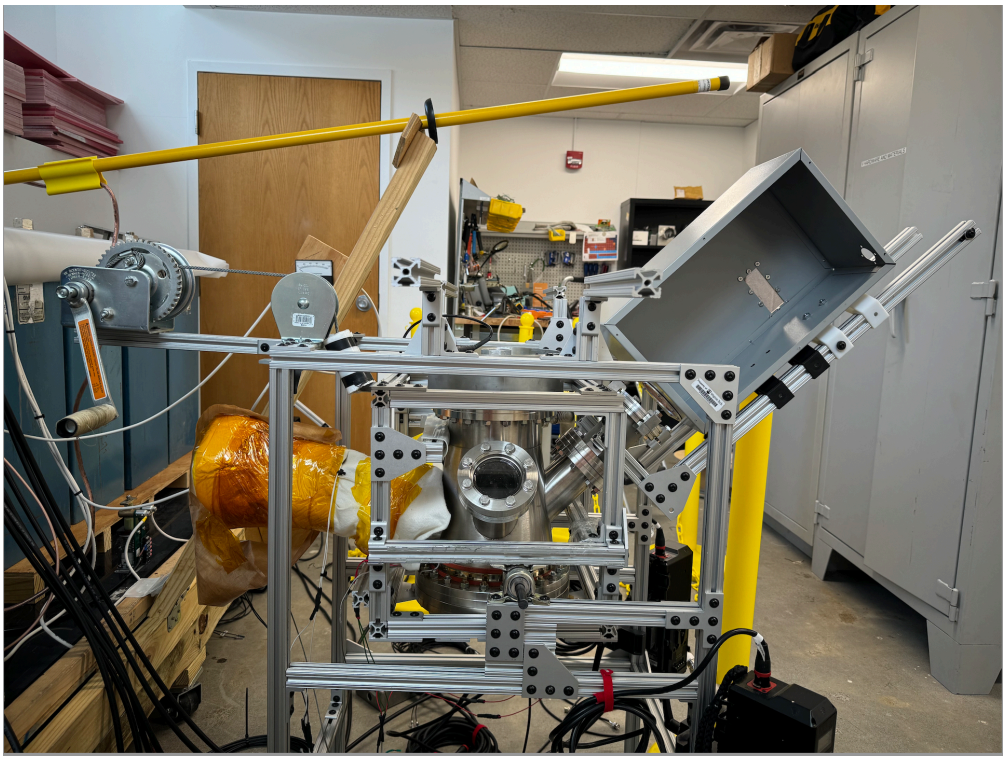

Figure 2.4: Side-view of chamber, as part of the experimental setup. The camera would ordinarily be placed in the Faraday cage on the right, and the viewport in the center is used as a place to allow light to enter the chamber on trigger. The insulated cylinder on the left is the reservoir where the metal is stored in its solid state when not being used in a trial.

The experiment is run remotely from outside the testing room due to inherent risks from the high potential to which the capacitors are being charged. There is a risk of electric shock and an acoustically hazardous air arc when the energy involved exceeds 10 kJ. This amount of energy can create a loud, potentially harmful explosion-like sound due to the rapid discharge of electricity, which can pose a danger to hearing or cause other injuries if a person is within close to medium range of the experiment [43]. Multiple safety controls, training protocols, and demonstrated proficiency benchmarks were implemented, and all were strictly adhered to. These included the mandate that the experiment is only run with two people who are certified in CPR and electrical safety, as well as various controls in the circuit that allowed it to run only when the door to the testing room is closed.

Additionally, the experiment is run in vacuum conditions. There is a vacuum line that extends from the side of the chamber to the vacuum system, which is capable of a 60 L/min pumping rate. The experiment is run at an operating pressure of 30-50 mTorr, which is considered a rough vacuum.

Chapter 3

Particle tracking efforts to ascertain core contamination

3.1 Experiment Description

A pulse forming network (PFN), made up primarily by a bank of capacitors, was the instrumental method by which the currents were delivered to the liquid metal. The liquid metal was exposed to current pulses of around 100 kA. The capacitors delivered this current when charged to a voltage of around 7 kV. This research is concerned with analyzing how the liquid metal reacts in these conditions, which will inform the usage in the context of z-pinch fusion devices.

Current is delivered from the PFN to a wire that is partially submerged under the surface level of the liquid metal. A diagram of the current path is shown in Figure 3.1.

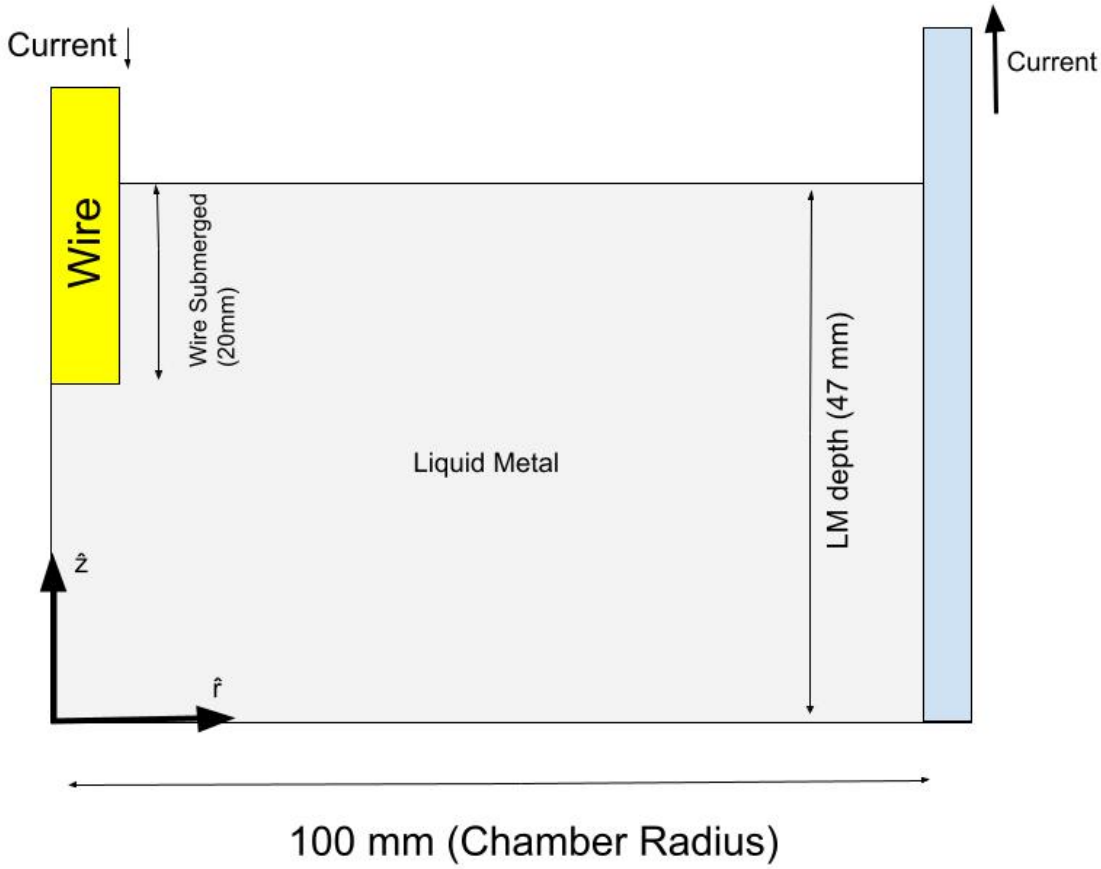

Figure 3.1: Path that current takes entering and leaving the chamber the current enters through the wire, moves down to the base of the chamber, and out via the walls and to ground.

When exposed to this current, an annular shaped liquid jet is formed. This is consistent among all of the trials which resulted in a proper discharge of the capacitor bank. Along with the annular jet, small droplets of liquid 'shoot' upward from the region (shown in Figure 3.2) immediately around the wire as well. These particles are referred to as 'ejecta'.

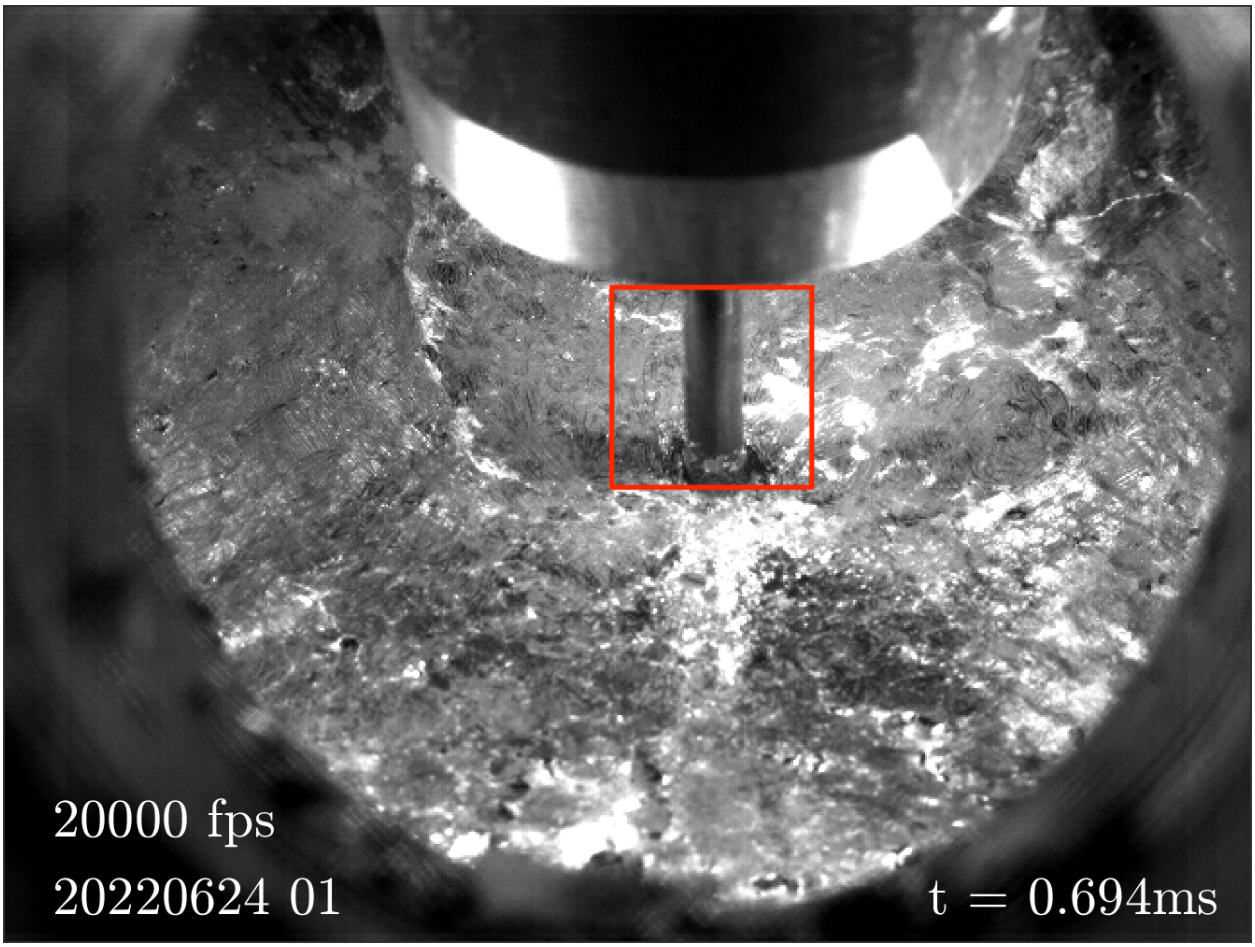

Figure 3.2: Region around wire as seen in the liquid metal chamber which is used as an area of interest in particle tracking efforts.

Generally, these ejecta travel upward in projectile trajectories from the surface of the liquid around the region of the wire, not usually following the path taken by the annular jet. Due to a lighter mass, these ejecta travel at velocities larger than the jet as well. This moving background and shifting illumination causes complications in tracking these particles. There exists a short window of time wherein these ejecta can reliably be tracked, in an experiment that is set up to investigate the early-time response of liquid metal behavior.

3.2 Ejected Droplets

Upon visual analysis of image data, sourced from the high-speed camera that is mounted on the experimental rig, it is clear that there are multiple forms of these ejecta. Most commonly, they show up either as a cloud of smaller, fine droplets, or as slightly larger distinct droplets. Figure 3.3 depicts ejecta as distinct particles.

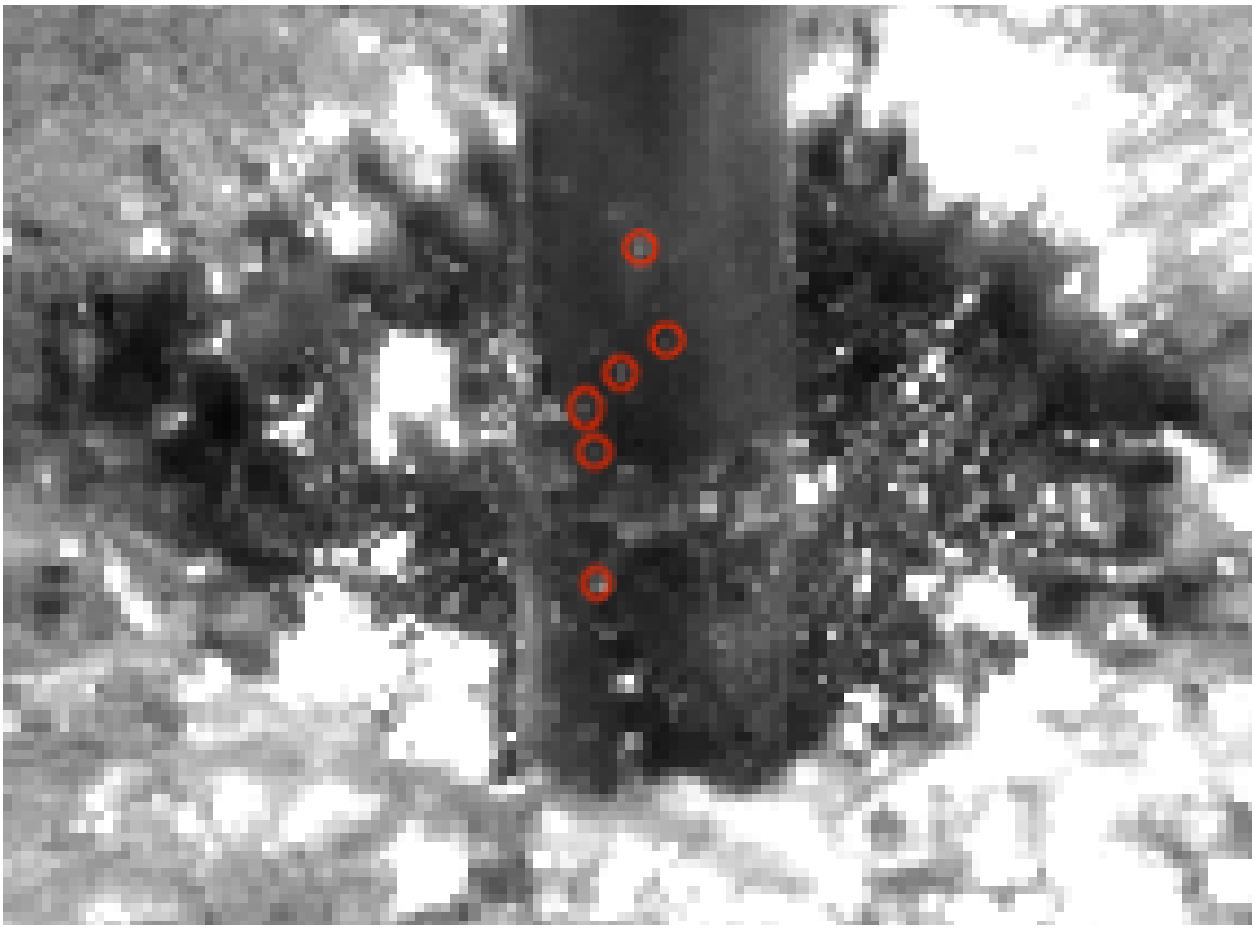

Figure 3.3: The particles circled in red are the ejecta particles that need to be tracked. As noticed, there is very little, and varying, contrast with the background. Only the particles within the region around the wire are tracked as the background makes the ejecta particles 'pop' out when the images are properly processed.

As seen in Figure 3.3, these ejecta can take different forms. They also have various diameters,

and while spherical geometry is assumed for the purpose of analysis, there is no one shape type that these ejecta appear.

The most plausible reason regarding the formation of these particles is that they are formed from the region directly around the wire that is partially submerged in the liquid metal. The current pulse may cause these particles to form early in the timeline of each experimental run. Sufficient impulse could be delivered to the liquid metal near the wire to cause ejection at higher initial speeds.

Electrostatic forces may also play a role: while no charge associated with the particles have been measured, electrostatic repulsion in a high current environment may become significant, which additionally expedites the ejection of these particles from the larger pool[4]. Also, under vacuum conditions, vapor pressure and thermal agitation face less resistance.

Finally, it is also important to note that during LEX operations, the heaters are disconnected for five to ten minutes before the experiment is actually run. This is to prevent an induced potential from the ground loop that exists between the heater circuits and the charge/dump circuits which deliver the current. As a result, there is no accurate measurement for the temperature at which the liquid metals are exposed to the current, or the variation in cooling rates (though it can be approximated that a decrease of 5 K in the pool between the time when the heaters are disconnected, and the current is pulsed through).

Later in this thesis, there is a discussion on some engineering work that was done in order to upgrade the capabilities of the experimental rig. This was done in order to enhance control over what temperatures the apparatus could be run at. For both lower temperatures (filling in the 'gaps' from previous testing campaigns), and higher ones, there are predictions that have been made in previous bodies of work [17] regarding the variation in ejecta masses at different points. It can be predicted that at higher temperatures, lower masses of ejecta

might be seen, but with higher velocities. There is also a small probability that the higher energy due to elevated temperatures actually cause a higher mass of ejecta to be expelled as well. Having experimentally tested values for these ranges of temperatures can allow us to reasonably extrapolate the severity of core contamination when the liquid metals are used in fusion reactors, which run significantly hotter [6].

3.3 Theory of Algorithms Utilized

Most of the data that is gathered is in the form of images, recorded by a high-speed camera. This camera is mounted at an angle facing down into the chamber, and high-powered lights mounted on either side help provide a glimpse of the reaction of the liquid metal when exposed to the electric current. A schematic of this is shown in the Experimental Design section of this manuscript.

While the intensity of the high-powered lights are imperative to viewing the bulk movement of the liquid in such a short span of time, they also make it difficult to track the ejecta particles. The ejecta particles are already small and move in a different direction than the annular jet. The movement of the jet blocks light from reaching the ejecta to view all of them properly, and the light that does penetrate impedes proper view of the background, which can make everything seem like one blended liquid pool. The following row of images in Figure 3.4 shows a more preliminary tracking method, which found edges on certain ejecta moving across a sequence of images from one shot of the experiment.

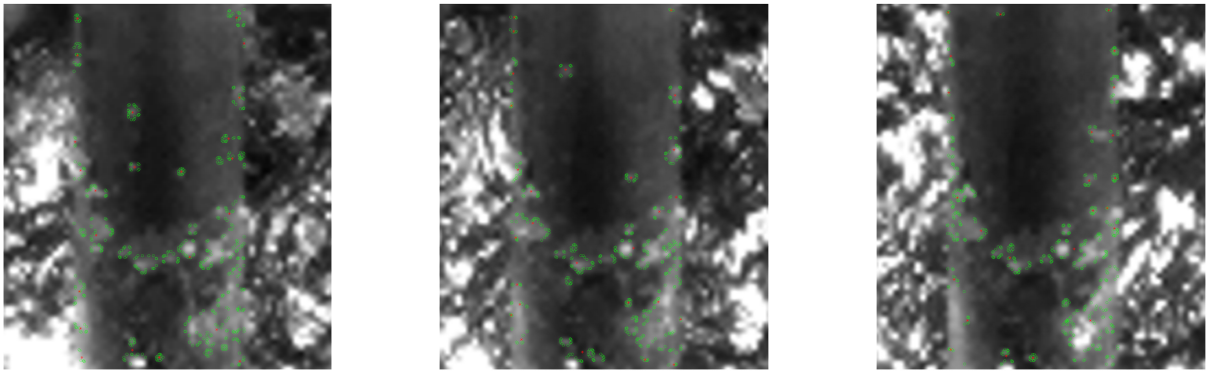

Figure 3.4: Edge tracking method applied on a test dated June 24th, 2022. The green markers are populated around particles that have enough of a difference in intensity with the surrounding pixels. The green markers are used instead of lines as the density of markers is used in later steps to calculate the centroid (shown in red).

In order to reliably track these ejecta, the images need to be processed. The bulk of the tracking depended on the ability to sift through the noise (of which there is a considerable amount), and 'pop' out the ejecta points based on the differences in light intensity.

3.4 Image Processing

The image processing sequence was developed as a combination of different methods, applied in succession on a series of images. For most of the shots run with the camera recording at 30,000 frames per second, only the first 3.33 ms is reviewed. Visual analysis made it clear that after this point, the light is blocked by the annular jet, and the ejecta have probably passed from view of the camera. The first hundred shots from the raw data are fed into a MATLAB code, and stored as image data. From there, it is indexed at 1-100, and run through a loop, each iteration of which performs a number of actions designed to get the ejecta in more prominence, so it can be tracked.

First, the code resizes the image. Visual analysis shows that both the clouds and the in-

dividual ejecta particles form around the region of the wire, as discussed earlier. For each of the six different shots that were studied, a different crop sized was used, due to different camera configurations and volumes of liquid.

For the purposes of this thesis, an experimental image sequence captured on June 24, 2022 was focused on. To enhance the resolution for detailed analysis, the original image was resized to 2.5 times its initial dimensions. Following this, a region of interest using the bounding box defined by the coordinates (x = 840.51 px, y = 477.51 px) for the top-left corner and dimensions with the width at 149.98px and height at 166.98 px was cropped. This processed image highlights the specific area under investigation, as shown in Figure 3.5.

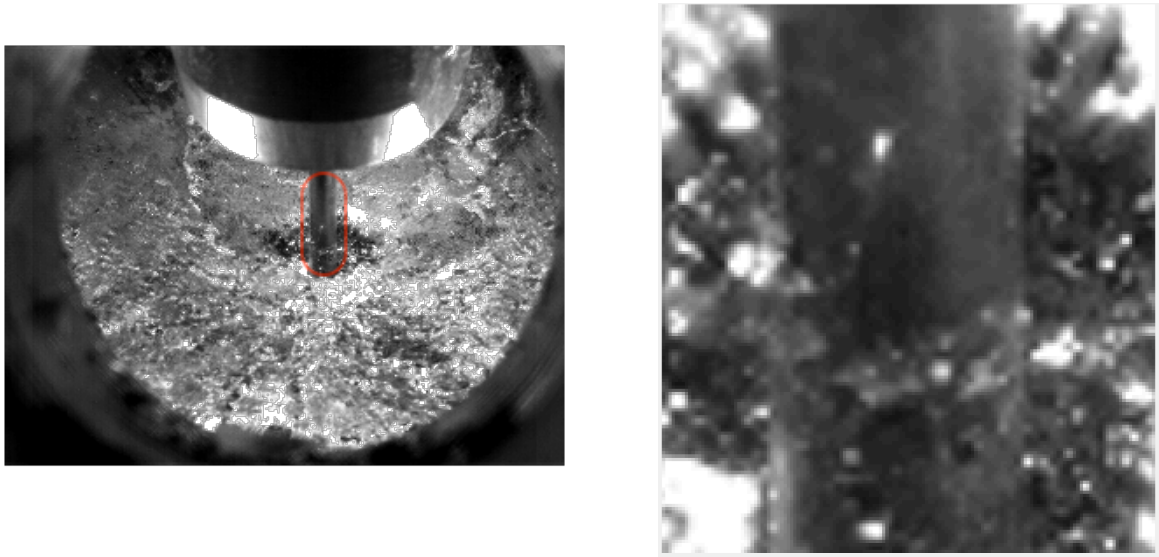

Figure 3.5: Image resizing for better view for a test performed on June 24th, 2022, utilizing the tenth image shot. The image on the left is the raw image data captured by the camera, and the image on the right shows the region of interest used in this study. Thus region is highlighted in the red oval within the image on the left.

In earlier attempts at analysis, the following methods were applied before the image was resized, but it was realized that performing the qualitative parts of the analysis (the parts that focused on manipulating the pixel values in order to make the ejecta more visible)

worked better when the image was resized prior to the start of the entire process.

After resizing, the Contrast Limited Adaptive Histogram Equalization (CLAHE) method was applied on each of the images [18]. The CLAHE algorithm has a few steps, but essentially, the image is divided into different 'tiles.' Usually, a 512x512 image is resolved into 8x8 pieces. Then, a histogram of the images was computed, which shows the distribution of the pixels in the images by the intensity. The resized image's histogram is shown in Figure 3.6, next to the histogram after the CLAHE algorithm is applied, both computed from the 55th frame of the June 24th, 2022 trial.

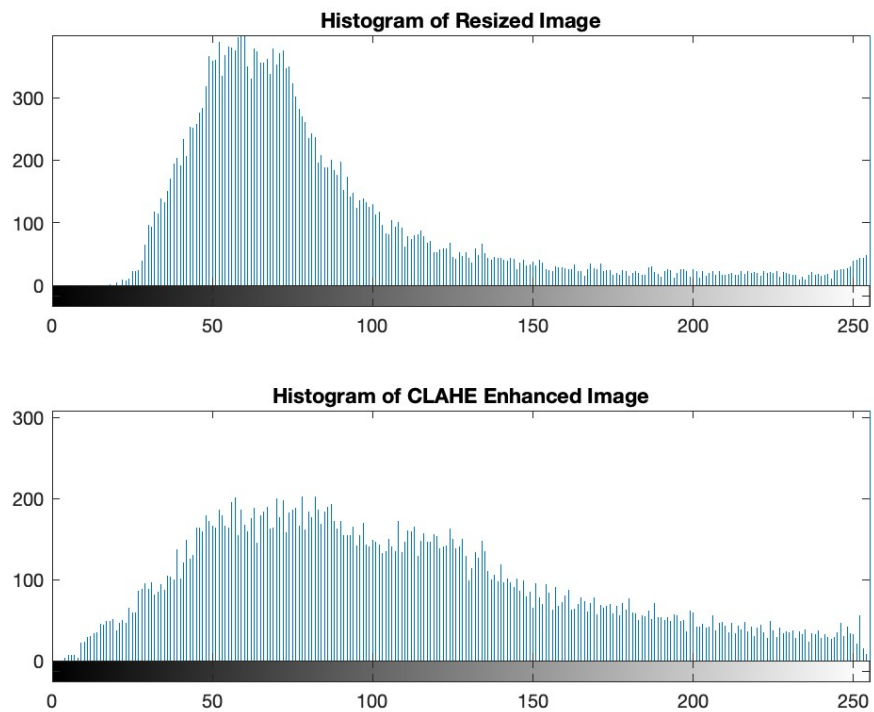

Figure 3.6: Histograms associated with initial denoising of images using CLAHE Algorithm, the 'smoothing' effect on the pixel intensities is clearly depicted.

The histogram is clipped at a certain level to control the noise amplification. The histogram is clipped at 1% of the total pixel count within it's corresponding tile to control contrast enhancement and prevent noise amplification. In this clipping process, any histogram bin

that exceeds the 1% threshold has its excess pixel values redistributed across other intensity levels within the local region, ensuring no single intensity range becomes overly dominant. A Cumulative Distribution Function (CDF) is created from the histogram, as shown in Figure 3.7. The curve of the CDF shows us that the original image had a plurality of pixels that fell within the same range of intensities (shown in the steep curve in Figure 3.7). When the CLAHE algorithm alters the image, the distribution is much more uniform. Once this is computed, the CDF is normalized, and bi-linear interpolation is used to smooth over the differences between the tiles to ensure a clean processed image.

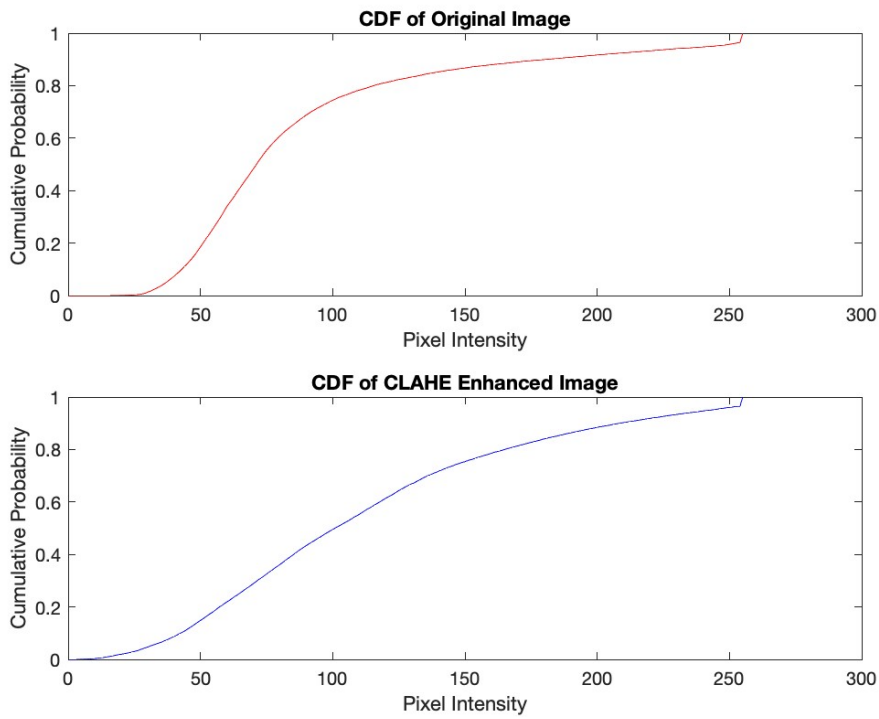

Figure 3.7: CDF of image before and after CLAHE algorithm is applied. The top plot shows pixel intensities which are concentrated in a narrow range, resulting in poor contrast. The bottom plot shows that the algorithm redistributes pixel intensities more evenly by applying localized contrast adjustments and limiting histogram amplification to prevent noise amplification.

Once this step is completed, the image is put through a neutral-density (n-d) filter. A n-d filter was chosen due to its inclusion of robust convolution-based filtering. This filter

works for this application due to later emphasis on edge detection and boundary effects that require handling. Convolution is a general purpose technique for image processing [19]. The 2D discrete convolution equation within the context of image processing is given by:

$$J(x,y) = \sum_{m=-k}^{k} \sum_{n=-l}^{l} h(m,n) \cdot I(x-m, y-n) \tag{3.1}$$

where *J(x,y)* is the output image, I is the input image, *h(m,n)* is the kernel (filter) coefficient at the positions of m and n, and k and l are the half-width and half-height of the filter respectively [20]. For all of these calculations, the MATLAB programming language was used. The n-d filter made use of this syntax, using the in-built imfilter function:

```
mean_image = imfilter(grayImage, fspecial('average', [15,15]), 'replica');
```

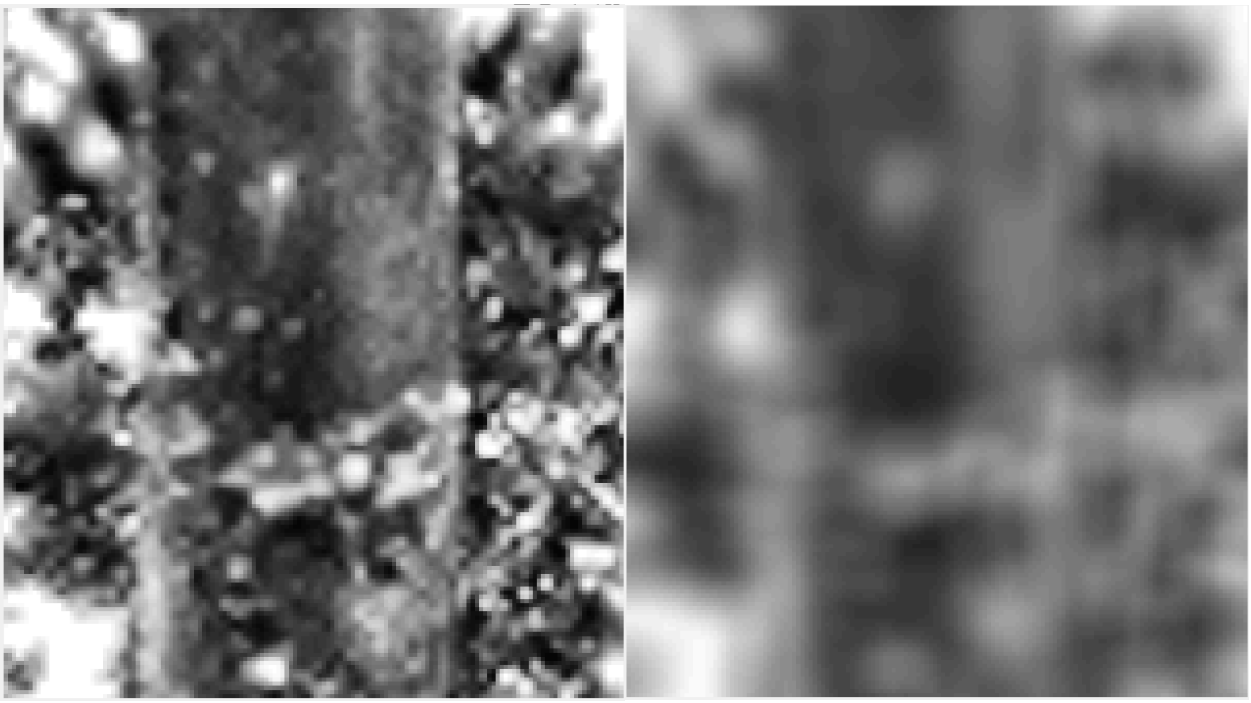

Figure 3.8: CLAHE enhanced image (left) and N-D filtered image (right). The image on the right demonstrates the effect of a N-D filter, which reduces image brightness and smooths intensity variations without enhancing local details, resulting in a blurred appearance with reduced contrast and definition.

The change between the image when the CLAHE algorithm is applied and the Neutral-Density filtered image is shown in Figure 3.8.

As discussed, in this case a mean filter was applied. It uses a 15x15 kernel, and averages the intensity values for all the pixels within that kernel. The mean filter was chosen over a Gaussian filter due to computational times, and a greater ability to reduce random noise. Additionally, the next step involves subtracting the difference of the N-D filtered image from the CLAHE enhanced image. This step was more effective when used on a mean filter than a Gaussian filter, demonstrated by visual analysis as shown in Figure 3.9.

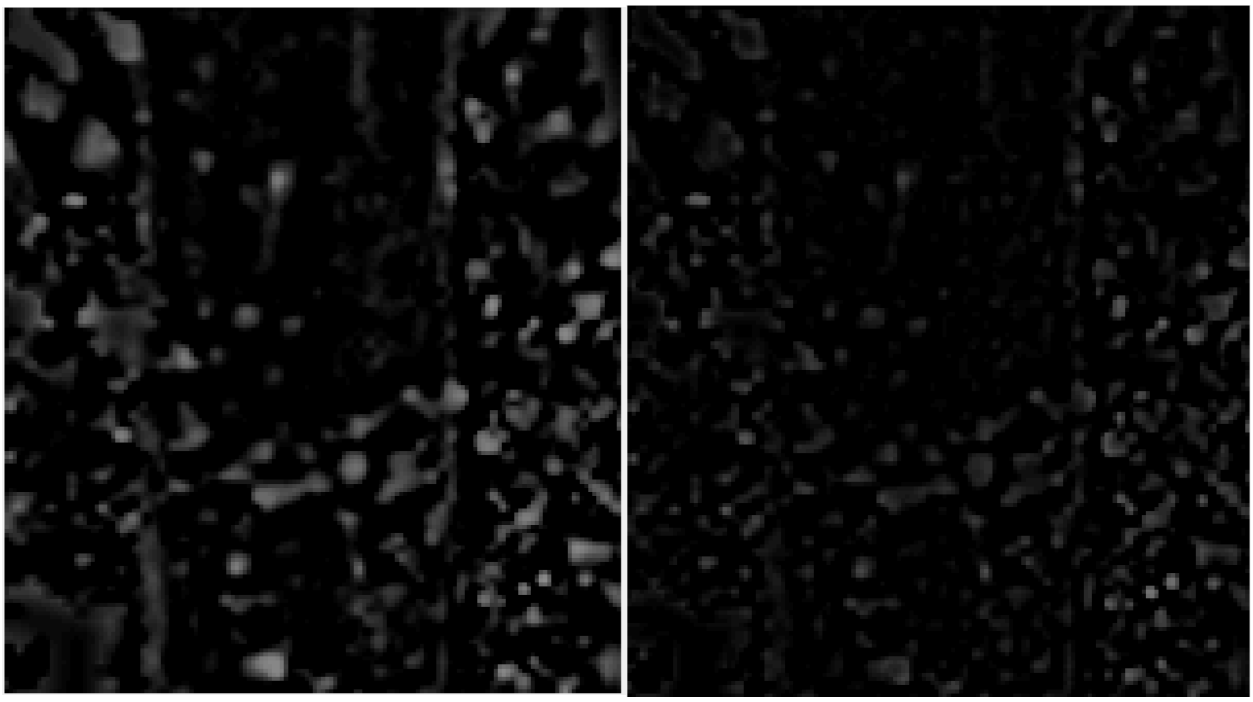

Figure 3.9: The image on the left displays the result of applying a Mean Filter for subtraction, which smooths the image by averaging pixel values over a uniform window, leading to less localized smoothing and more block-like artifacts. The Gaussian filtered image on the right uses Gaussian-weighted kernel, resulting in more natural blurring and a gradual transition between pixel intensities. While the Gaussian Filter typically preserves finer details, the Mean Filter can be advantageous when the primary goal is to reduce high-frequency noise uniformly across an image, leading to a more generalized smoothing effect).

This image was then binarized in order to make the particles 'pop' out. This is shown in Figure 3.10.

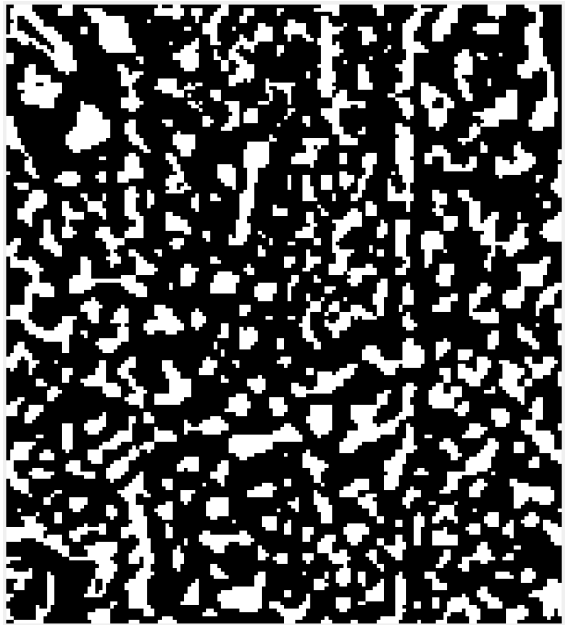

Figure 3.10: Subtracted figure, binarized. As seen, the variations of the light intensities are more easily observed. This is a crucial step in setting up the images that later aids in the calculations of the ejecta positions. In this image, the white regions are more likely ejecta particles, which will be confirmed in subsequent steps.

Once the image is binarized, it is sent through a median filter. The median filter splits the image into 3x3 localized blocks around each pixel, and the median intensity inside those blocks is computed. The central pixel's intensity is then changed to be that median value. Median filtering is useful to reduce noise while preserving edges [21] (which informs the use of later methods in order to compute ejecta positions. The noise variance of the median filter for an image which contains noise can be given at [22]:

$$\sigma^2_{\text{med}} = \frac{1}{4nf^2(n)}\sigma_i^2 \approx \frac{\sigma_i^2\pi}{n + \frac{\pi}{2} - 1} \tag{3.2}$$

where σ_i^2 is the input power, n is the size of the median filter mask (in this case, 3x3), and $f^2(n)$ is the noise density function.

The median filter helps us smooth over the noise. The variance in the intensity of the pixels between the images with the neutral density filter subtracted from the original image, and these ones with the median filter applied on top are shown in Figure 3.11 over frames 55 to 100 within the same test on June 24th, 2022.

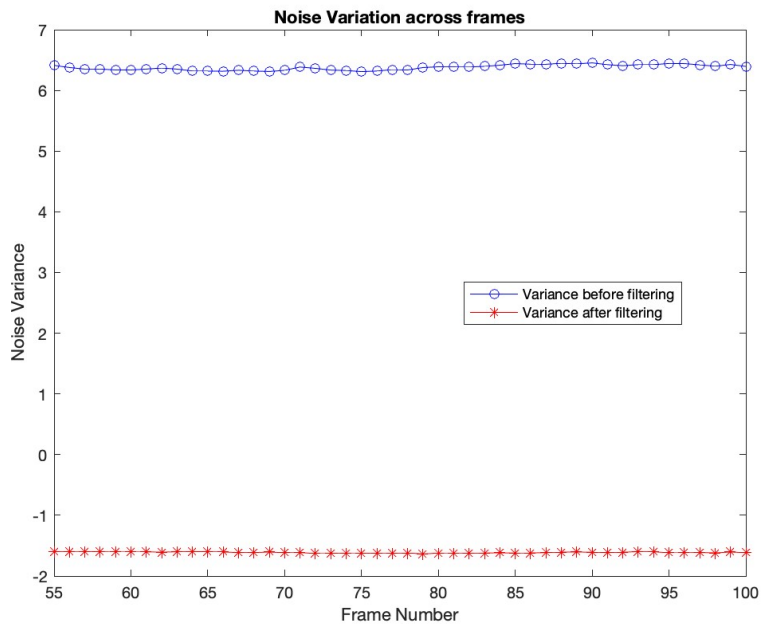

Figure 3.11: Noise variation across frames, logarithmic scale. The red curve, which shows the noise variance after filtering, is substantially lower, demonstrating the effectiveness of the median filter in reducing high-frequency noise while preserving critical image details such as edges.

A visual representation of the images used in the comparative analysis above is shown in figure 3.12.

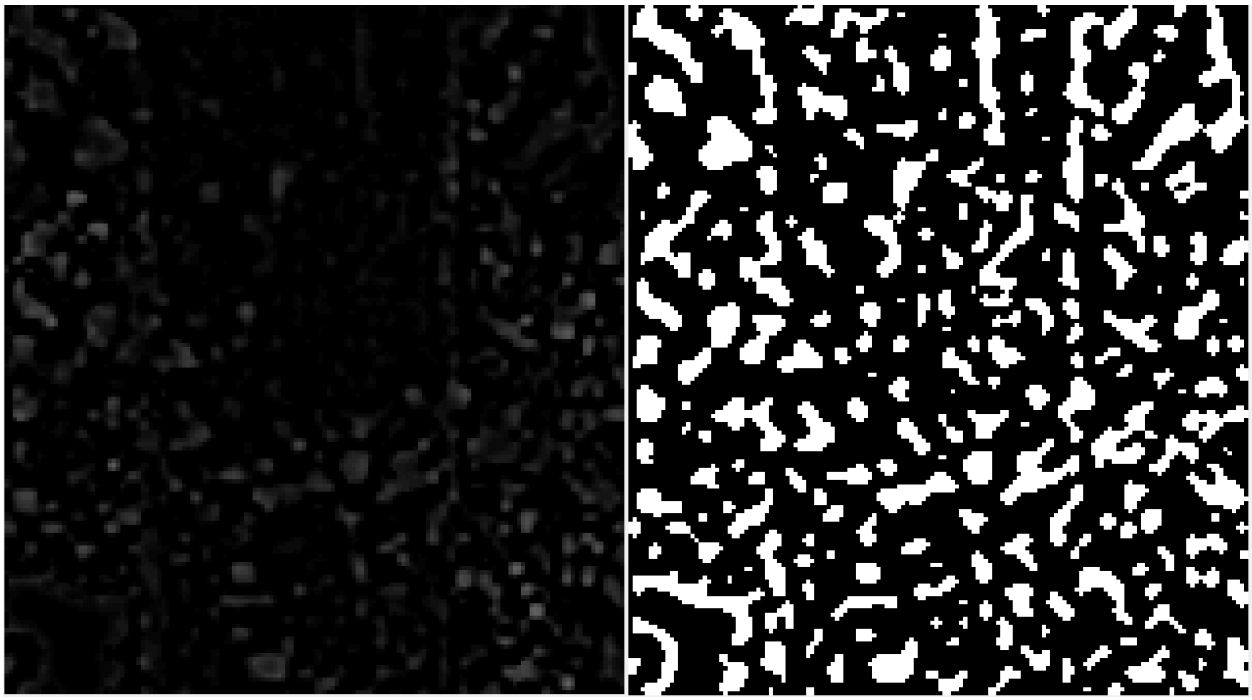

Figure 3.12: Subtracted image using mean filter (right), and binarized image put through the median filter (left).

3.5 Calculation of Ejecta Positions

The previous subsection delved into the set-up portions of the automatic ejecta tracking efforts. While a lot of the noise is reduced, a lot of noise is still captured by the methods laid out in this section. To combat this effect, later portions of this thesis will discuss data analysis efforts that sift through the noise and return the position data of interest to this project. In this subsection, the ejecta tracking sequence will be continued from where it left off at the median filter.

Once the image is run through the gauntlet of procedures laid out in Section 3.4, it is resized by a factor of 10 before it is displayed as output, so that visual confirmation of the code's efficacy is possible. While the analysis focuses on the region of the wire, there is still some

noise on the sides outside of the region of the wire. The annular jet is still moving while these droplets are moving upward. To handle this noise, a region of interest was chosen for the rest of the sequence to work within, so that the dynamics of the bulk movement do not interfere with the tracking of the ejecta. This is shown in Figure 3.13.

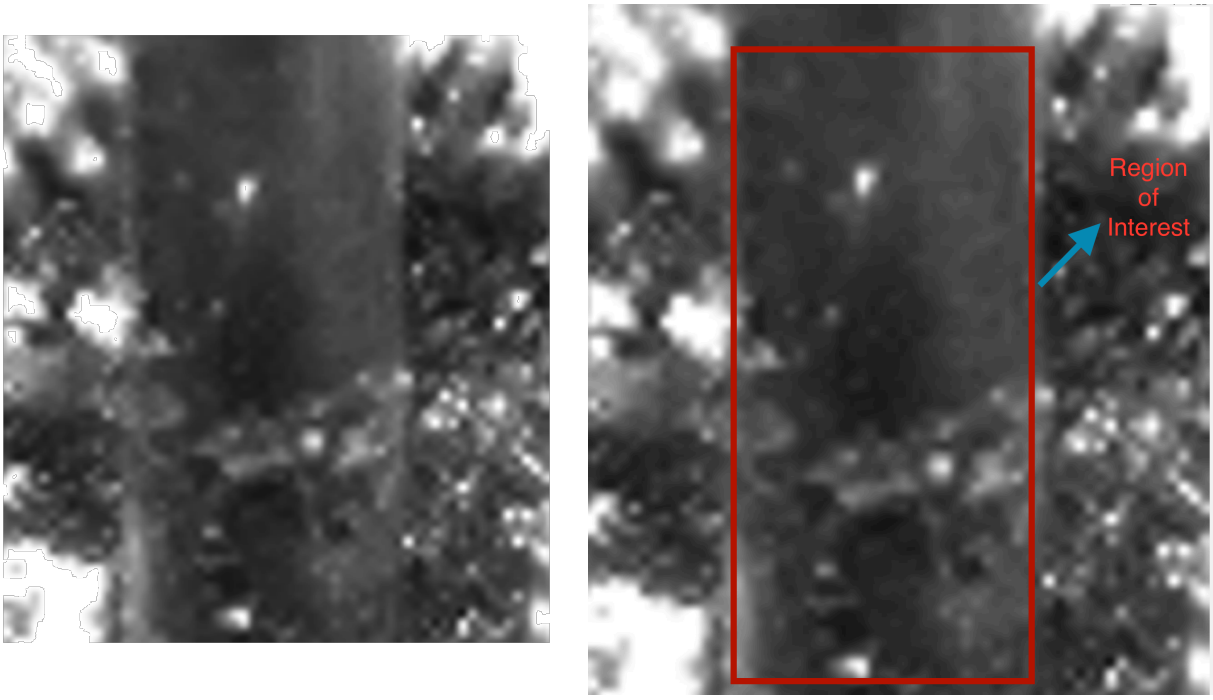

Figure 3.13: Selection of Region of Interest for calculations. This is the region within which most ejecta are observed over a significant number of frames.

The image shown in Figure 3.13 is in the original form. The images used in the following calculations are more like those shown in Figure 3.12. For more visual checks, and also to make this job easier for the sequence, a blending action (explained later in this subsection) is applied, which combines the images shown in Figure 3.13, and the one in Figure 3.12. This method was chosen as it helps to ensure that the edge detection used later on only picks up the points that are of substantial interest. Figure 3.15 shows the composite image that is produced.

If an image is treated as a continuous function, the following expression can be used to

quantify the similarity between two images, at a time t, integrated over the domain U (both images) [22]:

$$\varepsilon(t) = \frac{1}{2} \int_{\mathcal{U}} (f(x, y, t) - g(x, y, t))^2 \, dx \, dy \tag{3.3}$$

Linear interpolation is widely used in order to blend two images. The process is linear as it combines the intensities of two pixels. An adapted expression (from work done in [23]) for this is shown here, where A and B are the input images, and C is the output for the blended image. The blending factor is designated as α, which for the MATLAB implementation used in this work is 0.5, as both images contribute equally to the blend, shown in equation 3.4.

$$C(x, y) = \alpha \cdot A(x, y) + (1 - \alpha) \cdot B(x, y) \tag{3.4}$$

The inputs, as well as the results of the blend operation, are shown in Figures 3.14 and 3.15. The blend uses color to highlight the differences in intensity between potential ejecta points and the largely static background of the wire, as shown in Figure 3.14.

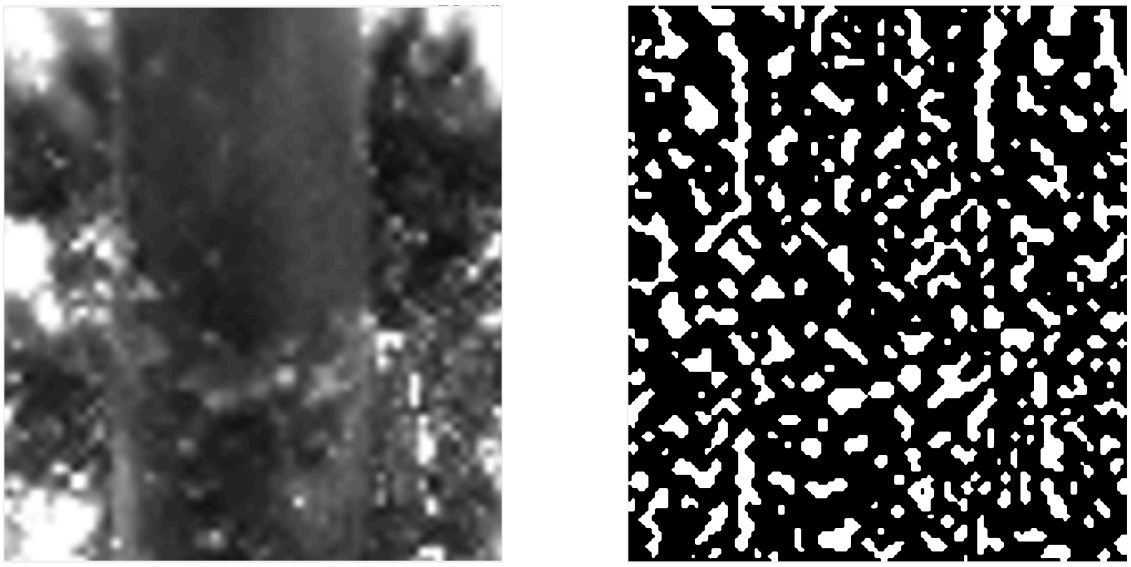

Figure 3.14: Input images for blend operations using linear interpolation.

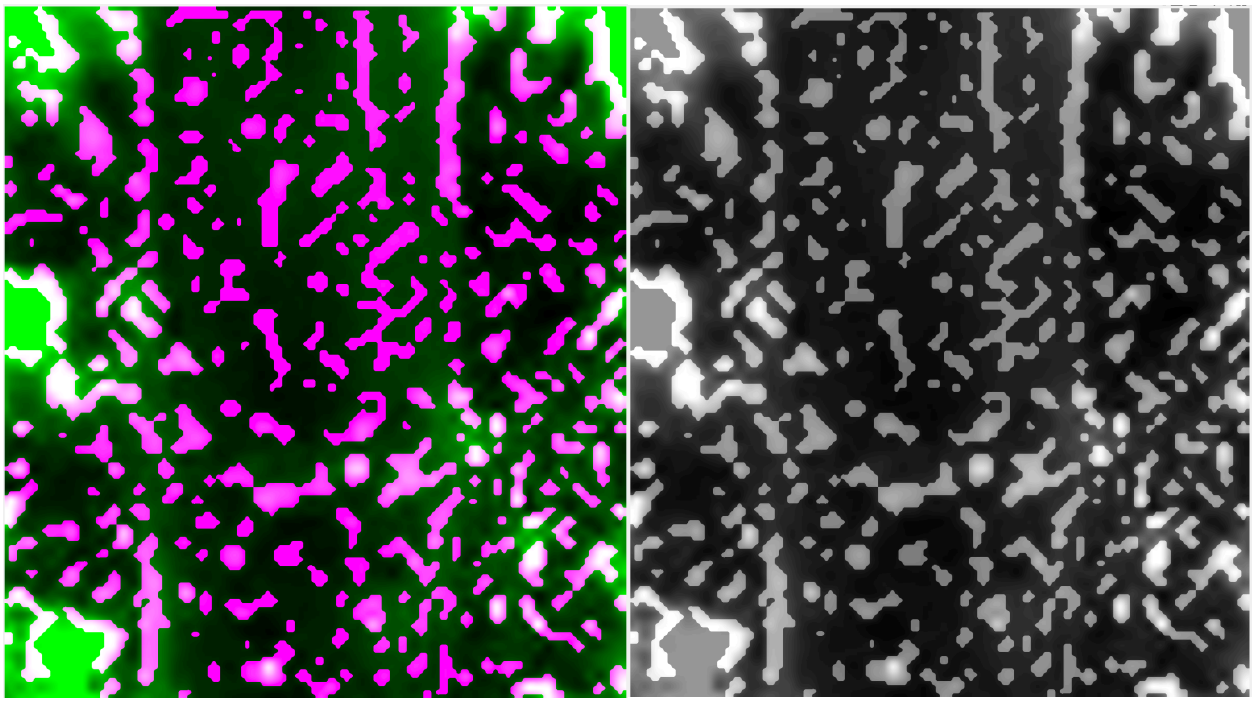

Figure 3.15: The image on the left represents the result of blending two input images using linear interpolation. The blending factor ($\alpha = 0.5$) ensures that both input images contribute equally to the output, allowing the visibility of intensity variations in both regions. The purple and green colors are used to show the regions which are clearly at different intensity levels than their immediate surroundings. The image on the right is the corresponding grayscale version of the blended output.

When these two images are blended, the output image as shown in Figure 3.15 is instrumental in the ejecta calculations, and also works as a 'sanity check' in regards to the code working the way it should. The blend is important as subsequent steps rely on edge detection. It can be seen that there is a clear change in pixel intensity between the purple regions and the immediate surroundings, which is a good indicator for the edge of a particle. The image is converted to grayscale as the edge detection algorithms used later are better suited for those kinds of images, rather than the color ones the blend output produces.

The image on the right in Figure 3.15 is the one that is used in the main portions of the tracking sequence. The pre-processing laid out in this paper was selected after comprehensive literature reviews of image processing methods used throughout the past few decades, and after an exhaustive campaign of trial-and error with the test cases selected for this work (mainly, an experimental run on June 24th, 2022, performed by Dr. Daniel Weber).

The histogram of the light intensities between the original image, and the one at the end of the image processing sequence is shown below in Figure 3.16.

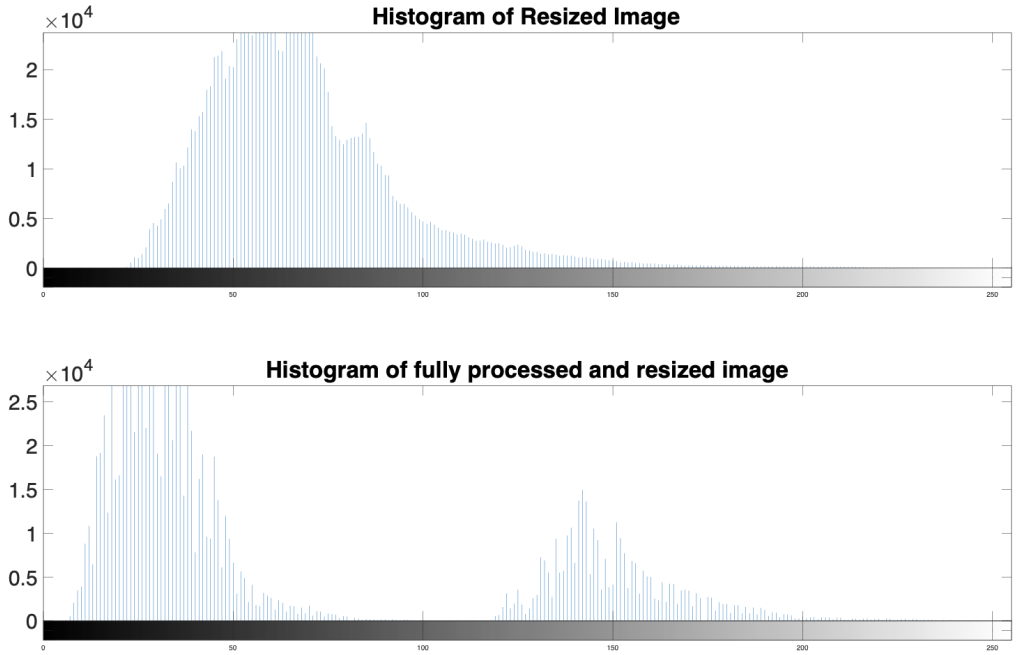

Figure 3.16: Comparison of pixel intensities before and after processing methods are applied. The processed image (on the bottom) shows a more evenly distributed range of pixel intensities that indicates improved separation between background noise and potential ejecta regions. This distinction in intensity levels is beneficial for classifying ejecta particles.

The comparison shown in Figure 3.16 provides a clear picture regarding the effectiveness the sequence. The noise shown in the middle of the graph is split into two different intensity ranges instead of one for most of the pixels. This is important as the differences in light intensity are used in order to classify the ejecta properly. With only two distinct light intensities being recorded, it is possible to clearly distinguish between the background noise and the points of actual interest

Once the blended image is computed, an edge detector is applied. In this project, the Sobel method for edge detection is implemented. In image processing, a kernel is a small matrix, that is used to apply certain convolution operations, for example blurring, sharpening, and edge detection, to an image. Mathematically, a convolution operation given an input image

and a kernel is given by Equation 3.5. The matrices used as kernels specifically for Sobel Edge detection are given by S_x and S_y, as shown here [24]:

$$S_x = \begin{bmatrix} -1 & 0 & 1 \\ -2 & 0 & 2 \\ -1 & 0 & 1 \end{bmatrix}, \quad S_y = \begin{bmatrix} 1 & 2 & 1 \\ 0 & 0 & 0 \\ -1 & -2 & -1 \end{bmatrix}$$

Figure 3.17: Sobel filters for edge detection in the x and y directions

For the Sobel edge detection algorithm, the Sobel operator is the magnitude which is computed by the gradient of S_x and S_y

$$M = \sqrt{S_x^2 + S_y^2} \tag{3.5}$$

where the partial derivatives of S_x and S_y are the following, computed with C=2:

$$S_x = (a_2 + Ca_3 + a_4) - (a_0 + Ca_7 + a_6); \tag{3.6}$$

$$S_y = (a_0 + Ca_1 + a_2) - (a_6 + Ca_5 + a_4). \tag{3.7}$$

The Sobel edge detector was chosen over the Canny method for edge detection (both of which are popular in the image processing community) for a few reasons. Most importantly, the Canny method uses Gaussian smoothing, which, as discussed earlier, was not as effective as using the Contrast Limited Adaptive Histogram Equalization (CLAHE) method. The Canny method was tried in this sequence, but the nature of the input images, which are alredy pre-processed, did not comport with the inherent pre-processing steps that the Canny method demands.

The kernels shown above for S_x and S_y are applied as masks for each individual pixel. The magnitude is calculated throughout the image. The pixels where the 'M' values are higher

suggest significant shifts in intensity between pixels, while the lower values suggest more smooth changes. The pixels are threshold-ed against a certain value of 'M', values above which are marked as edge pixels. A paper by Gao et al. [25] wrote down a set of criteria that the Sobel method follows in order to make its edge particle determinations. The threshold value is given below, where rows and columns refer to the number of rows and columns in the images, respectively. For the test case used in this work, the processed image is a 1664x780 image. The original image is in the 480x640 image.

$$\text{Threshold} = 4 \times \sqrt{\frac{\sum_{i,j} M^2(i,j)}{\text{rows} \times \text{columns}}} \tag{3.8}$$

Each pixel's magnitude is compared with these two condition groups. The pixel must qualify one of the two conditions. The first one corresponds to the vertical top and bottom directions from the pixel, and the second corresponds to the horizontal left and right directions:

Condition Group 1:

$$M(x,y) > \text{Threshold} \tag{3.9}$$

$$M(x,y) > M(x,y-1) \tag{3.10}$$

$$M(x,y) > M(x,y+1) \tag{3.11}$$

Condition Group 2:

$$M(x,y) > \text{Threshold} \tag{3.12}$$

$$M(x,y) > M(x-1,y) \tag{3.13}$$

$$M(x,y) > M(x+1,y) \tag{3.14}$$

The gradients for each pixel are calculated and shown overlaid on Figure 3.18.

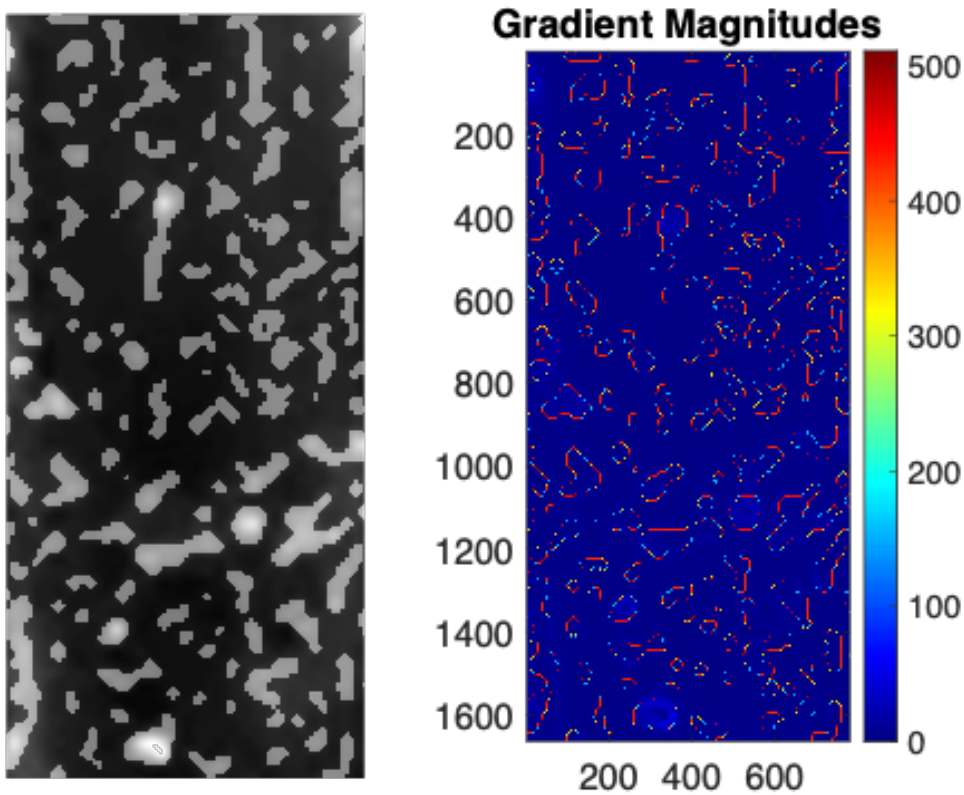

Figure 3.18: Gradients calculated using Sobel kernels for edge detection, shown on the right.

The directions of the Sobel gradients are also important. They can help in feature detection in future steps, as the computer will rely on those gradients in order to track the edges across different frames. The direction of the gradient, expressed as the angle θ is given by [26]:

$$\tan\theta = \frac{y}{x}. \tag{3.15}$$

As such, the gradient directions can also be visualized, as shown in Figure 3.19 where the darker colors signify more sharp boundaries that are classified as edges, and whether they are moving in the vertical or horizontal directions.

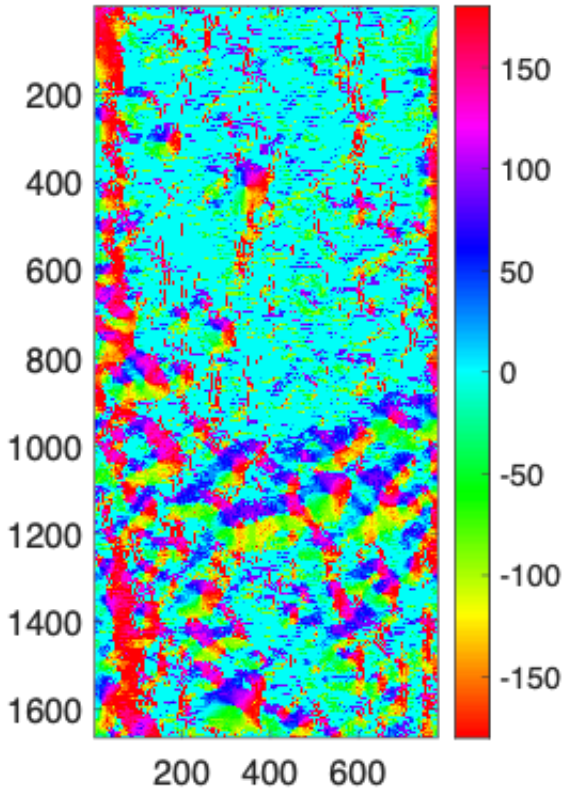

Figure 3.19: Gradient calculation directions of the processed image. The darker colors (indicated on the larger numbers in the color bar) correspond to stronger edges, which indicate potential ejecta particles.

The image with the results from the Sobel edge detector is shown in Figure 3.20, zoomed in on the right for clarity.

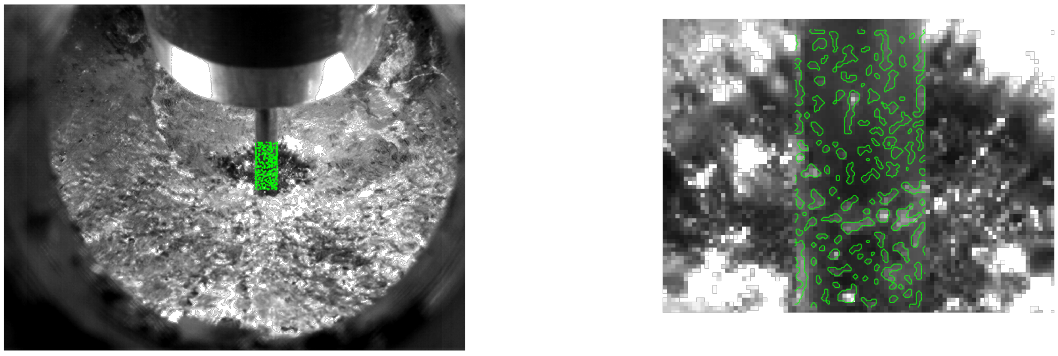

Figure 3.20: Results, after Sobel method of edge detection is applied.

Once the edge detection is completed, the corresponding edge point coordinates for each frame are stored.

Once this is done, there exists a large array for each image that contains the edges as well. A MATLAB function named *bwconncomp* is applied. This function is designed to find and count connected components in binary images. This is derived from a widely used method in image processing known as connected component labeling, which is an application of fundamental graph theory concepts.

Two non-background pixels p and q can be said to belong to the same connected component if there is a sequence of p pixels (i.e $p_o, p_1, p_2, ..., p_n$) such that $p_o = p$, $p_n = q$ and p_i is a neighbor of $p_i - 1$ [27]. Essentially, the definition of a connected component depends on its immediate neighbor, in both the horizontal and vertical directions. To make this tracking more robust, a sub-concept known as *8-connected* was availed.

The 8-connectivity concept says that every pixel is connected to its eight immediate neighbors on all sides, it looks like this [28][29]:

$$\begin{bmatrix} x & x & x \\ x & 0 & x \\ x & x & x \end{bmatrix}$$

For a pixel located at (i,j), the 8-connected neighbors are:

- **Horizontal Neighbors:**
  - $(i, j-1)$ (left)
  - $(i, j+1)$ (right)
- **Vertical Neighbors:**
  - $(i-1, j)$ (top)
  - $(i+1, j)$ (bottom)
- **Diagonal Neighbors:**
  - $(i-1, j-1)$ (top-left)
  - $(i-1, j+1)$ (top-right)
  - $(i+1, j-1)$ (bottom-left)
  - $(i+1, j+1)$ (bottom-right)

When computed in this manner, a visual representation of the output of the connected components can be seen in Figure 3.21.

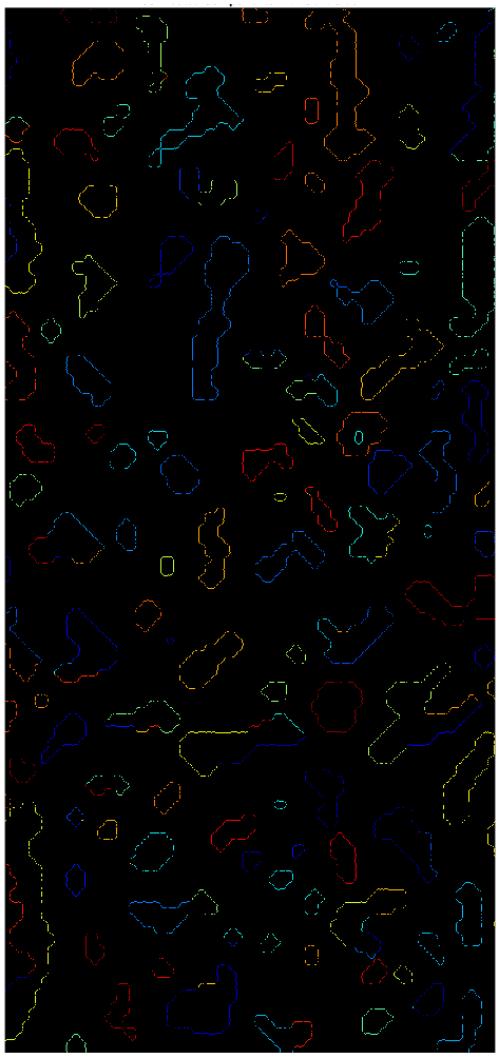

Figure 3.21: Visual representation, when edge components are connected using 8-connectivity connected-component labeling. Previously calculated edge pixels were connected in order to depict the edge of each ejecta particle as a whole.

These edges are now the connected components, which are used to track across frames. The connected components are stored as a MATLAB structure array. For example, for the 60th image on the experimental run conducted on June 24th, 2022, the following data is stored:

```
    cc =

  struct with fields:
```

```
    Connectivity: 8
       ImageSize: [1664 780]
      NumObjects: 196
    PixelIdxList: {1×196 cell}
```

This shows that 196 components were connected using the 8-connected method. To extract more data to inform the final steps of this tracking effort, the areas bounded by these edge trackers are treated as different 'blobs.' Each 'blob' is represented by a single point, its centroid, and those centroid points are eventually stored as position data to be used in velocity calculations. MATLAB's *regionprops* function is used to extract information relating to the center of mass.

Centroids are fixed points that can be considered the geometric center of a region [30]. While the edge and connected points computed earlier do move similarly across frames, the particles tracked are composed of liquid metal. As such, there is a lot of variation on the boundaries due to the loss of liquid as the particles move. This necessitated the calculation of the centroids, which will help track the particle as a whole, negating the risk of miscalculated outputs due to the boundary's continuous changes.

If there is a region with N pixels (i.e N(x,y)), then the Centroids are: C_x and C_y are given by [31]:

$$C_x = \frac{1}{N}\sum_{i=1}^{N} x_i \tag{3.16}$$

$$C_y = \frac{1}{N}\sum_{i=1}^{N} y_i \tag{3.17}$$

The centroid particles are shown overlaid on the raw image in Figure 3.22. The centroid particles are the red dots, shown within the green bounded regions (which are the edges).

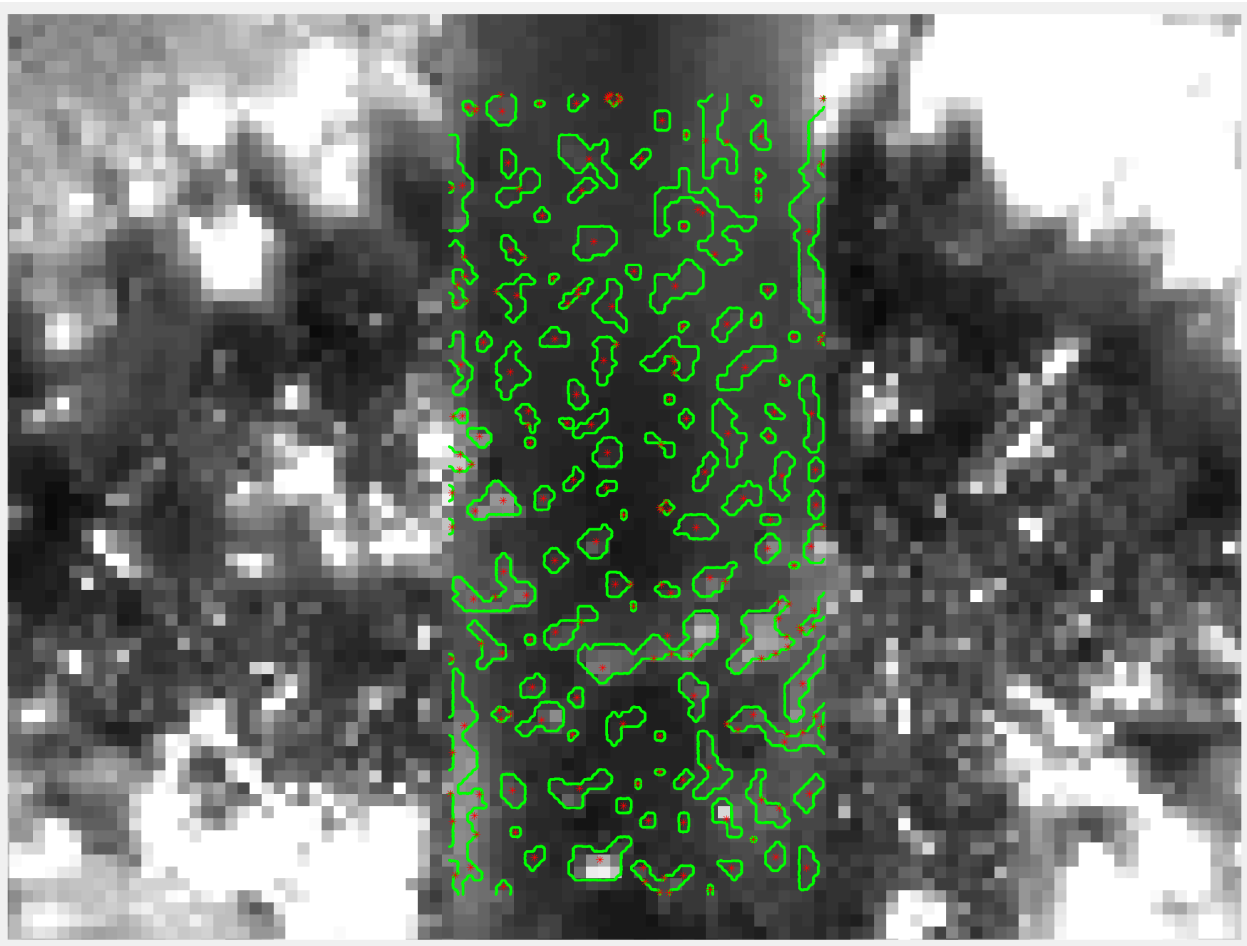

Figure 3.22: Edges and centroid, calculated for the 60th frame of an experimental run on June 24th, 2022.

The *regionprops* function also calculates the area of each of the edges formed after the individual components are connected, which is required to find the mass of the ejecta particles. This is done by using the number of pixels within each bounded area. For a labeled region L (taken from the connected component labeling method used earlier), and m and n, the area of the region bounded by the connected edges can be given by [32]:

$$A_k = \sum_{i=1}^{m} \sum_{j=1}^{n} [L(i,j) = k] \tag{3.18}$$

The areas are important in later steps to sift through the droplets being tracked, in order to only track ejecta that are moving across the sequence of images. The analysis still returns a lot of points which are not ejecta, but just byproducts of the light intensity changes due to the movement of the bulk liquid. The histogram shown in Figure 3.23 is a depiction of average area of the tracked edges, taken from data across all forty-five analyzed frames.

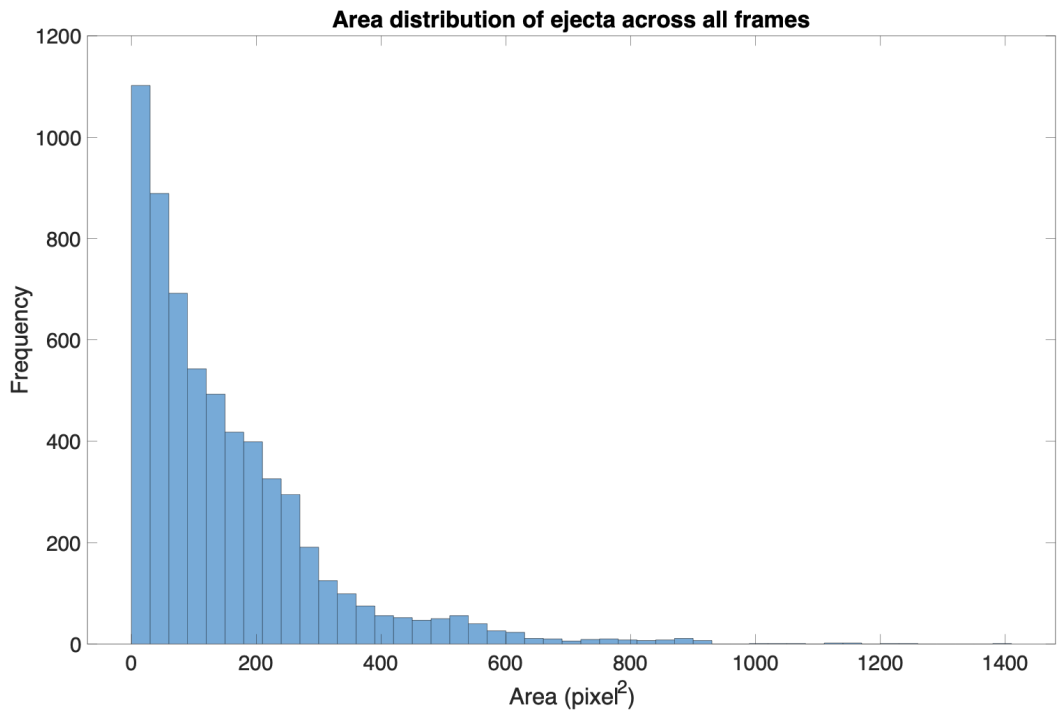

Figure 3.23: Area sizes of tracked edges, across all frames.

Figure 3.23 shows the range within which most of the edges are calculated. There are a greater number of smaller particles than larger particles that are being tracked. Most of the particles are within 0–20 pixels^2 in area. This is because the centroids are calculated, and then scaled back to the original size of the image. In the scaled and processed version, the

majority of the regions bounded by the connected edges would have areas under 250 pixels^2.

3.6 Results

The analysis laid out in sections 3.4 and 3.5 is looped over all the frames of each experimental shot. The next step is to sift through the distinct position data, group those that are close to each other across successive frames into ejecta points. This data will be fed into a separate system (explained in subsequent subsections) which will calculate the velocities of the ejecta particles.

One of the main ways to group ejecta points together is to analyze the distances traveled by the centroids across frames, using two-point correlation. This method of 2-point correlation is mainly used in the field of astronomy to measure of the probability that there will be two galaxies within a fixed distance of each other. Applying this technique here will allow us to guide our software in recognizing that points close to each other are the same object to track [33].

The two-point correlation function being implemented generally takes the following form:

$$\text{Two-point correlation index} = \frac{\text{Histogram of distances}}{\text{Expected counts}} \tag{3.19}$$

The expected counts are found by multiplying the density of points and the area of an annular ring between the two points. To plot the histogram, the distance between any two points i and j on a 2D grid is calculated (in order to find the probability of having two particles close to each othe) using equation 3.20.

$$d_{ij} = \sqrt{((x_i) - (x_j))^2 + ((y_i) - (y_j))^2} \tag{3.20}$$

To calculate the 2-point correlation, a slightly different method to track centroids was used. This method used the Features from Accelerated Segment Test (FAST) algorithm. This algorithm uses the pixel locations of the centroids of the ejecta points. When used, the method takes in a threshold value, and checks a circle of a certain radius around that pixel for brightness levels above or below that threshold. If I_p is the intensity of the pixel being analyzed, and t is a threshold value, this piece-wise method in Equation 3.21 is used to determine the edges of the correct particles [34][35]. In this equation, S_{p-x} represents the status of a neighboring pixel relative to a central pixel p, with possible values of d (darker), s (similar), or b (brighter). I_{p-x} and I_p are the intensity values of the neighboring and central pixels, respectively.

$$S_{p-x} = \begin{cases} d, & \text{if } I_{p-x} \leq I_p - t \quad \text{(darker)} \\ s, & \text{if } I_p - t < I_{p-x} < I_p + t \quad \text{(similar)} \\ b, & \text{if } I_p + t \leq I_{p-x} \quad \text{(brighter)} \end{cases} \tag{3.21}$$

This method does carry over some noise, but does provide a more varied range from which the average distances are based. The noise can be visualized in Figure 3.24, but a clear peak is also visible. The pixel radii are also taken from the grid of the cropped and fully processed image, before those values are scaled back to the grid of the original image.

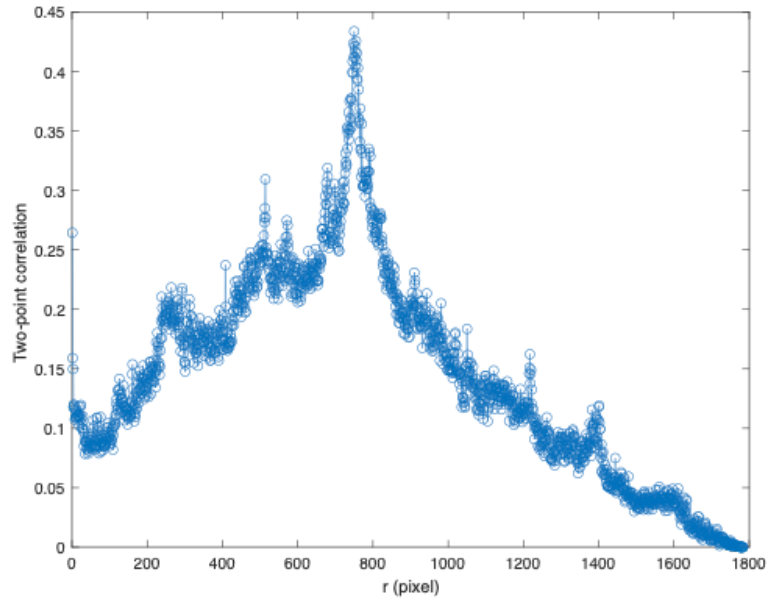

Figure 3.24: This graph shows the 2-point correlation of the centroid distances. It showcases the centroids which are most frequently observed by the code. 2-point correlation finds the probability of finding two points within a certain distance of each other.

The points of interest in this analysis are the peaks observed in the graph. These peaks indicate the most frequent instances of centroids being detected within specific annular radii. They specify the pixel distance within which the next calculated centroid is expected to be found. In this test, it appears to have been somewhere in the 700 pixel distance range. This is corroborated by the histogram, which shows the most frequent returns in a similar range.

The decrease in correlation on either side of the peaks in this plot indicates that the spatial correlation is strongest at those peaks and diminishes significantly for both smaller and larger distances. The correlation not settling down to zero at smaller distances suggests that there is still some degree of regularity in spatial correlation at these shorter distances. From the histogram, it can also be inferred that it is unlikely that the next closest centroid is further than 1000 pixels away. The effectiveness of this method is contingent upon employing the correct image processing techniques for each test. If the same method were applied to a

second test on the same day, it might not produce the requisite quality of data in order to track these ejecta across frames.

These data points are all stored for the next steps. All the centroid positions (x,y) and the frame number it is detected. The centroids are also scaled back to the original size of the image, as shown in Figure 3.24.

There are a number of techniques which are suitable to associate data [36][37][38][39][40]. In this work, a lot of the analysis' approach was customized to the output from the visual tracking sequence codes which were developed. The centroid data, which corresponds to the ejecta, were saved for each frame as distinct position points. This data was fed into another sequence.

This sequence's first step was to lay out clear parameters which corresponded to the area sizes, radii, and the distances between each point between frames which was calculated by the 2-point correlation shown above.

For example, for the test case used in this work, the parameters used were the following:

```
distance_threshold = 3;
max_frame_gap = 2;
upward_movement_threshold = 2;
```

Where the distance threshold is the maximum distance to consider points as the same particle, the max frame gap is the maximum number of frames to allow a gap in particle tracking, and the upward movement threshold is the minimum upward movement to consider the particle.

These pixel values are in the scale of the original image, as discussed earlier, which is a 480x640 grid. That explains the lower values of the threshold numbers. The distance is

calculated by the normal Euclidean distance formula, taking the differences between the x and y coordinates across frames and squaring it. The total distance is computed by the following equation [41]:

$$\text{total_distance} = \sum_{m=2}^{n} \sqrt{(x_m - x_{m-1})^2 + (y_m - y_{m-1})^2} \tag{3.22}$$

The next steps involve the code looping through the data table. the upward movement is calculated by:

$$\text{upward_movement} = \text{y_initial} - \text{y_final} \tag{3.23}$$

If a particle isn't tracked within two frames of the preceding one, it is no longer tracked, which ensures that there isn't much of the same observational variation that might have been present in more manual tracking approaches. There is also an inherent possibility of error due to the apparent centroid movement. Additionally, the velocities fluctuate depending on the time in the experiment when the tracking was conducted. The time can vary as there is a need to wait until when the ejecta are clearly visible to track. This impedes the ability to keep a lot of the variables constant between tracking.

Apart from all of these conditions, a particle needs to be tracked at least for more than eight frames. To try and counteract the time differences between different experimental shots for the sake of repeatability, the tracking must begin at some point in the first five frames that are being processed. These steps ensure some enhanced robustness in the tracking.

For the test case on June 24th, 2022, a screenshot from the classified particles, overlaid on the original image, is shown in Figure 3.25.

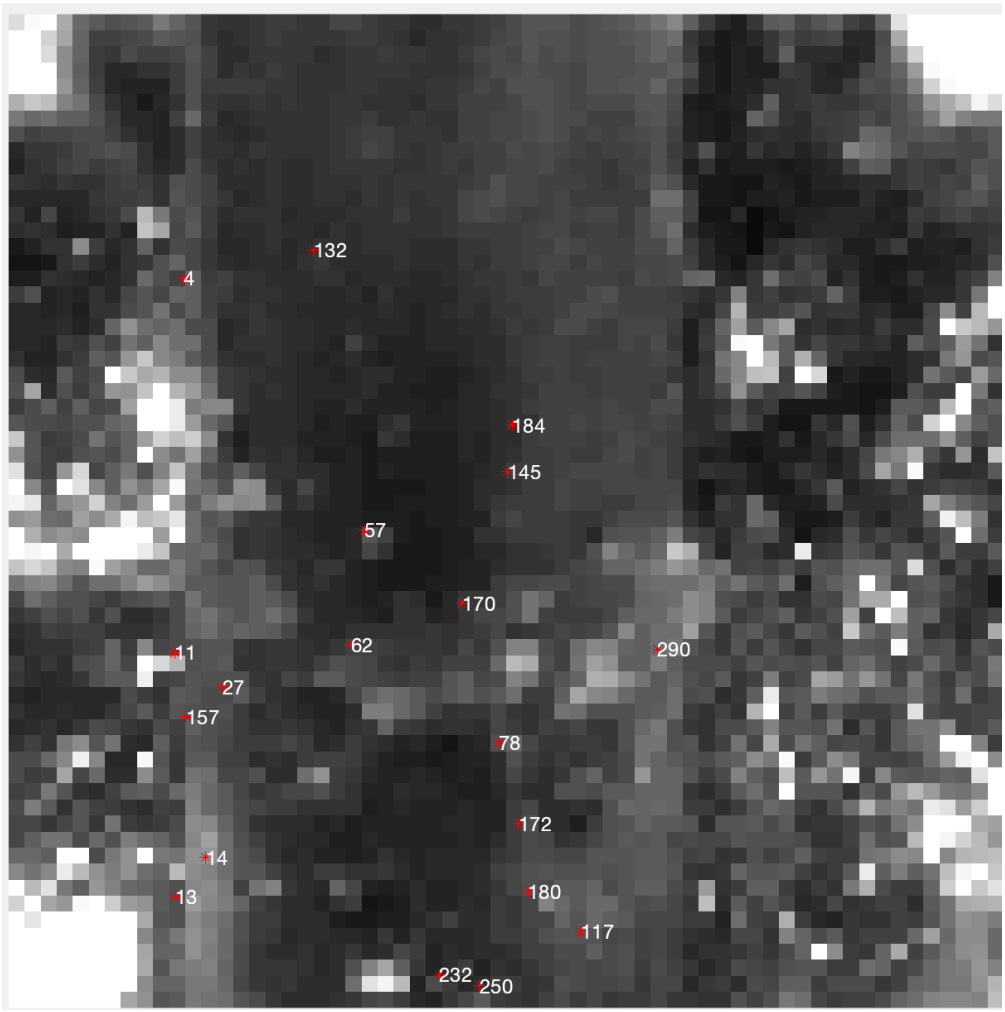

Figure 3.25: Tracked particles, in the sixth frame for June 24th 2022.

The code outputs different particle IDs for the initial grouping just using distance. The conditions applied whittles down the number of particles, but keeps the original particle IDs. Without any conditions, the code tracks hundreds of particles that are too close to each other. Each condition is also checked step-by-step to ensure proper identification of the ejecta. The trajectories of the few particles that are tracked at the end is shown here. The motion of the particles can be shown by plotting the trajectories, as shown in Figure 3.26.

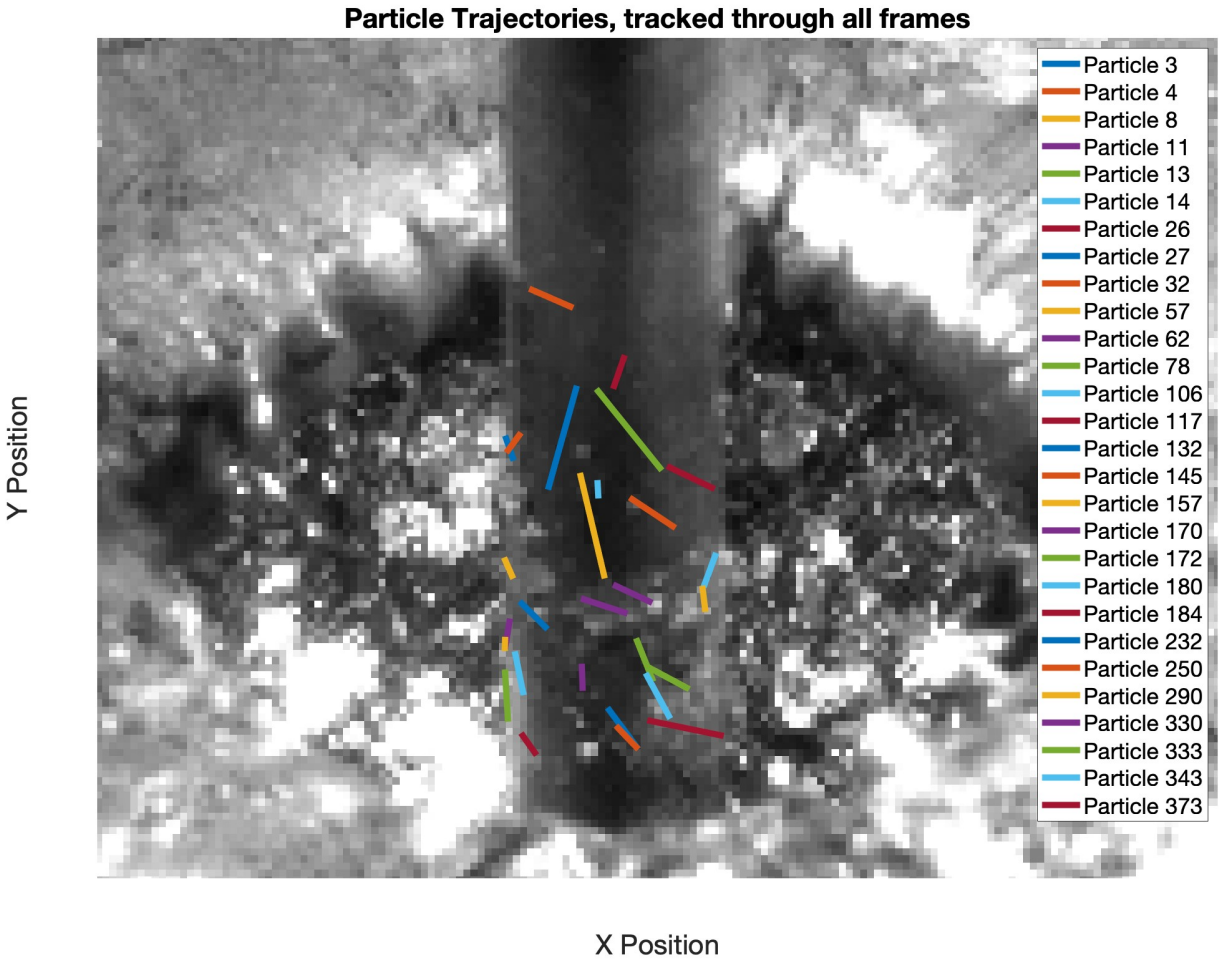

Figure 3.26: This plot shows the trajectories of particles that were tracked across all of the frames of this analysis.

Each color represents a different particle. There were 28 particles that were deemed fit to be tracked in this trial.

3.7 Comparison with Manual Tracking

This method was applied to seven different executions of the tests of the Liquid Electrode Experiment. The output was group position data, which tracked ejecta across frames in

pixels. Thanks to work done by Dr. Daniel Weber, there is data that converts these pixel values to SI units. The calculations for this code works on the same basic principles of Euclidian distance. The radius of each edge is averaged and fed into the computation as well (this is why this data was extracted in previous steps using *regionprops*. Once the SI unit data is computed, the differences between each frames are calculated and stored. The coordinates for the center of the page help in determining whether an ejecta is moving towards or away from the wire region, an the frame rate of the camera is used to find the time between each frame. The radial velocity and the z-direction velocities are calculated for each ejecta once position data is fed.

The mean velocities for each particle were tracked. The manual tracking effort that preceded this relied on visual tracking and estimation of position. In this work, over 300 particles were tracked over at least six frames each. If the upward directions can be taken as positive, the average velocity for the ejecta were shown to be 2.54 m/s, with a margin of error of 3.58 m/s. Manual tracking efforts showed some variation but were pretty consistent throughout, ranging from -1 m/s to 5.5 m/s.

The variation between the manual and automatic tracking could be due to a few reasons. Namely, the apparent centroid movement can lead to errors, as the noise is still very present when tracking visually. There is also variation due to the time at which the ejecta are identified. There is significant variation at when they are tracked due to the visibility requirements, which fluctuate immensely due to the random motion of the particles. This is somewhat mitigated in the automatic tracking, due to the inclusion of some conditions wherein the particles are all tracked within the same forty to fifty frames.

The formation of ejecta particles is not guaranteed. There are some tests wherein they form immediately, and others where they never appear. The graph shown in Figure 3.27 shows the likelihood of a droplet being formed at certain velocities by computing the bi-variate

probability density function of the ejecta velocities. It also uses the mass of the ejection to compute the probability of the droplet forming. There is some variation between the manual and automatic tracking, The manual tracking pegs the highest likelihood of ejecta formation at a velocity of 3.47 m/s in the vertical direction. The probability at this velocity is 1.0888%. The automatic tracking pegs this value at 1.14 m/s, but the probability is higher at 1.7850%. These maximum values are the highest probability of intersection with plasma fuel in a repetitively pulsed experiment.

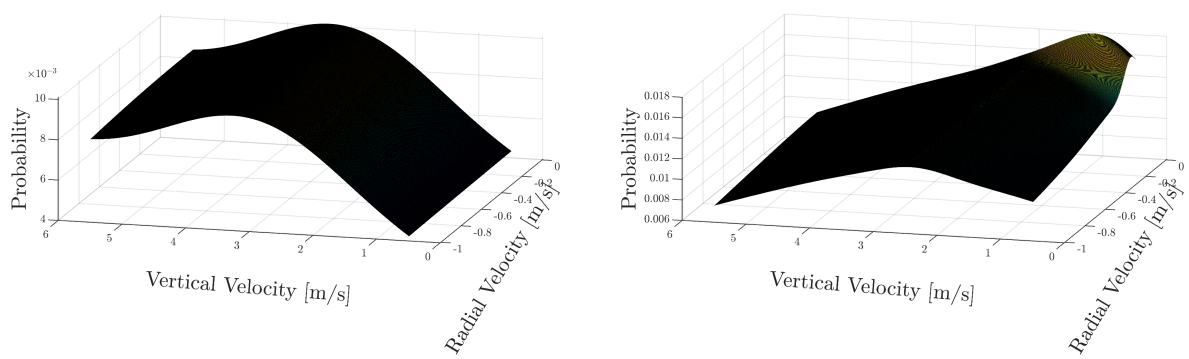

Figure 3.27: These plots show the likelihood that an ejecta particle will form, studied at different velocities based on the mass of each particle. The plot on the left is the result of manual tracking efforts, while the one on the right is derived from the automatic tracking efforts detailed in this Thesis. The manual tracking identified the highest likelihood of ejecta formation at 3.47 m/s, while the automatic tracking identified at 1.14 m/s.

There are some potential reasons for the discrepancy. There is a higher potential of errors due to apparent centroid movement in the manual tracking. There are also differences in the time at which movement was computed as ejecta were most noticeable at slightly different times in different experimental shots.

Nevertheless, ejecta pose contamination risks to the plasma fuel. The temperature of the liquid metal might also play a role in ejecta formation, and as such the next chapter discusses some experimental work that was done in order to set up a study of the heat dependency of the system. While it was not a focus of this thesis, it is a viable avenue to follow for future

research direction.

Chapter 4

Liquid Electrode Experiment Upgrade

One of the potential paths of investigation that was seriously considered was a study of the heat dependency of the system as a whole. As noted earlier, the temperatures were also used to calculate the viscosity and densities, which were in turn used to figure out the mass of the ejecta droplets.

This section will discuss some of the engineering work that was put into preparing for this testing campaign. Unfortunately, these efforts did not materialize to a substantial testing campaign within the duration of this Master's Thesis. However, it is an predominant part of the future work recommendations put forth in this research project.

The heat dependency of the system is an important aspect to investigate. The physical properties of the liquid metal vary heavily with temperature [44]. One of the reasons liquid metals are being studied are also due to their ability to manage heat fluxes [45]. As mentioned earlier, replicating a fusion reaction on Earth requires incredibly high temperatures [49]. The eutectic mix of tin and bismuth has a melting point of 411 K [47][48]. The motivation behind this work is to observe the likelihood of ejecta formation at different temperatures. There is a possibility that higher temperatures will lead to increased velocity of the droplets, and lower total mass being ejected. To achieve this, some modifications were required on the experiment. A part of the heating system (namely, the heater on the base of the chamber) was upgraded to meet the demand for not only higher temperature ranges, but also more efficient and quick heating.

4.1 Choosing a new heater and assembly

There are four heaters on the experiment. Two are each on the base of the reservoir and the chamber, respectively. Another is wrapped along the section connecting the reservoir and the chamber, while one runs along the base of the reservoir. The ones in the chamber are 250 W heaters, and the ones in the reservoir are 100 W. This is because the reservoir heats faster, and it is easier to concentrate the power in the chamber, where all of the experiment takes place. For all of the four initial heaters used, the maximum operational temperature was 450° Fahrenheit [50][51][52][53]. This covers the melting point and the operation range of the experimental data used in the particle tracking portion of this work. A PID controller is used to direct heat. Two thermocouples placed in the chamber and the reservoir provide information to the PID controller to make determinations on the output of the heaters. When upgrading the system, the PID controller could stay the same as it was rated to operate up to 1350° Celsius. The controller is shown here:

Figure 4.1: The image shows the PID (Proportional-Integral-Derivative) controller used to regulate the temperature in both the chamber and the reservoir during the experiment. The controller adjusts the output of the heaters based on feedback from two thermocouples placed in the chamber and reservoir.

The main challenges in finding the heater was to use one that fit in with the power input capabilities of the system that was to be replaced. The material of the heater was also changed from silicone rubber to a heater with a chrome steel sheath. The advantages of this include durability and resistance to corrosion [53] [54]. The material also provides greater thermal conductivity and has more structural integrity than the silicone heaters [55]. In the end, a Chromalox A-65 heater was chosen. It is a ring heater, and provides uniform heat distribution. The size of the heater (6" outer diameter) also is a good fit for the chamber base (which has 8" Outer Diameter) as well [56]. A picture of the heater is given in Figure 4.2 [57]:

Figure 4.2: This image shows the Chromalox A-65 heater selected for the experiment upgrade. The ring design ensures uniform heat distribution across the chamber.

To install this new system, the experimental setup was partly dismantled. A steel plate was cut to allow the ring heaters to protrude as it supported the heater to push against the base of the heater. Wires were soldered on the bottom of the heater to connect to the PID

system. The bottom of the chamber with the new heater system looks like this:

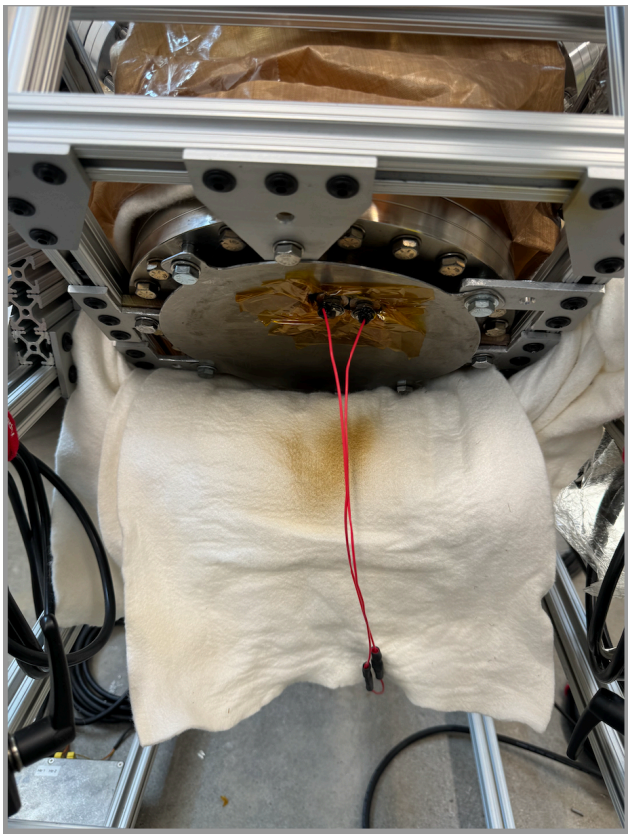

Figure 4.3: This image shows the bottom of the chamber after the installation of the new Chromalox A-65 ring heater. The wires shown are soldered to the bottom of the heater, which are connected to the PID control system.

One of the challenges with the last iteration of the heating system was the time it took to heat the chamber. To combat this, an insulation system of wool and PTFE-fabric sheets were wrapped around the chamber and the reservoir. The new heating system was tested and worked to heat the chamber faster, and was able to reach higher temperatures. The maximum temperature that this rig can reach is 393 K due to the temperature limits of the Torr-Seal.

Chapter 5

Summary

This thesis investigates the behavior of contaminant liquid metal particles in a simulation of Z-pinch fusion reactors, with a focus on their movement during electric current pulses. The research is motivated by the potential for nuclear fusion to serve as a sustainable and high-power energy source, and the role of liquid metals as self-healing plasma-facing components (PFCs) to enhance reactor performance and longevity. From an aerospace engineering perspective, there is notable interest in the usage of fusion reactors in spacecraft propulsion systems, enabling enhanced methods of exploring our solar system, and beyond [58].

The study is conducted within the framework of the Liquid Electrode Experiment (LeX) at Virginia Tech, which simulates the interaction of liquefied metal with plasma-like conditions through pulsed electrical currents and magnetic fields. By leveraging a variety of image processing techniques, this work tracked the ejection and movement of liquid metal particles under intensive conditions.

Key findings include:

- **Image Processing and Particle Tracking:** The study developed a robust image processing sequence using MATLAB, involving Contrast Limited Adaptive Histogram Equalization (CLAHE) and the Sobel edge detection method to accurately identify and track particle movement.
- **Experimental Design and Upgrades:** The experiment uses a eutectic mix of tin

and bismuth as the liquid metal, with a sophisticated heating system to maintain its state during testing. Upgrades to the heating capabilities are described, enabling precise temperature control for various test conditions.

- **Results and Impact:** The research highlights the significance of understanding particle dynamics to mitigate core contamination in fusion reactors. By analyzing ejecta behavior, the study informs strategies to optimize plasma performance and reactor design for sustainable fusion energy production. The average velocity was found to be approximately 2.54 m/s. While this number may appear smaller, it should be noted that the bulk of the data is recorded within the first few milliseconds. The time to wait in between each reaction, which does depend on the size of the test section, is crucial to limit the possibility of plasma contamination by droplet motion.

Chapter 6

Future Works

This project focuses on a small subset of techniques which aim to develop z-pinch fusion reactors. Fusion research has been facing challenges for several decades as there are fundamental problems which need to be solved to replicate the extreme conditions in which fusion reactions occur in the universe. This section summarized a recommendation provided earlier in this text for future work that can push the envelop on developing the requisite LM physics for z-pinch fusion reactions.

6.1 Heat Dependency of the System

As discussed earlier, a follow on study was proposed and an experimental setup was developed in order to investigate how the temperature of the liquid metal changes the behavior of the LM with regards to the objectives of z-pinch reactions. It can be hypothesized that the higher heat temperatures will result in faster ejecta velocities, but lower ejected mass.

Additionally, the temperature can also influence the LM's ability to absorb and dissipate heat, which reduces wall erosion. Further studies may also explore the interactions between liquid metal and plasma at varying temperatures, which could affect neutron moderation, impurity management, and overall plasma performance. This research will contribute to refining operational parameters, such as cooling rates and temperature control strategies, to enhance the sustainability of Z-pinch reactors.

Bibliography

[1] U.S. Energy Information Administration. (2023, August 21). Nuclear Explained - U.S. Energy Information Administration (EIA). www.eia.gov.

[2] Nave, R. (2019). Nuclear Fusion. Gsu.edu.

[3] Fasel, D., & Tran, M. Q. (2005). Availability of lithium in the context of future D–T fusion reactors. Fusion Engineering and Design, 75-79, 1163–1168. https://doi.org/10.1016/j.fusengdes.2005.06.345

[4] Subramanian, S., Wilson, A., White, C., K. Kontis, Evans, D., & Van. (2024). Tracking plume-regolith interactions in near-vacuum conditions. Physics of Fluids, 36(1). https://doi.org/10.1063/5.0180669

[5] Polsgrove, T., Adams, R. B., Fabisinski, L., Fincher, S., Dauphne, M. C., Miernik, J., Percy, T., Statham, G., Turner, M., Cassibry, J., Cortez, R., & Santarius, J. (2010, October 8). Z-Pinch Pulsed Plasma Propulsion Technology Development. Nasa.gov.

[6] Shumlak, U. (2020). Z-pinch fusion. Journal of Applied Physics, 127(20), 200901. https://doi.org/10.1063/5.0004228

[7] U. Shumlak, Adams, C. S., Blakely, J. M., Chan, B.-J., R.P. Golingo, Knecht, S. D., Nelson, B. A., Oberto, R. J., M.R. Sybouts, & G.V. Vogman. (2009a). Equilibrium, flow shear and stability measurements in the Z-pinch. Nuclear Fusion, 49, 7. https://doi.org/10.1088/0029-5515/49/7/075039

[8] Nian, V. (2017, January 1). Progress in Nuclear Power Technology (M. A. Abraham, Ed.). ScienceDirect; Elsevier.

[9] Kadomtsev, B. B., & Shafranov, V. D. (1983). Magnetic plasma confinement. Soviet Physics Uspekhi, 26(3), 207. https://doi.org/10.1070/PU1983v026n03ABEH004346

[10] Forbes, E. G., Uri Shumlak, McLean, H. S., Nelson, B. A., Claveau, E. L., Golingo, R. P., Higginson, D. P., Mitrani, J. M., Stepanov, A. D., Tummel, K. K., Weber, T. R., & Zhang, Y. (2019). Progress Toward a Compact Fusion Reactor Using the Sheared-Flow-Stabilized Z-Pinch. Fusion Science and Technology, 75(7), 599–607. https://doi.org/10.1080/15361055.2019.1622971

[11] U. Shumlak, Adams, C. S., Blakely, J. M., Chan, B.-J., R.P. Golingo, Knecht, S. D., Nelson, B. A., Oberto, R. J., M.R. Sybouts, & G.V. Vogman. (2009b). Equilibrium, flow shear and stability measurements in the Z-pinch. Nuclear Fusion, 49, 7. https://doi.org/10.1088/0029-5515/49/7/075039

[12] Badger, B., Abdou, M., Boom, R., Brown, R., Cheng, E., Conn, R., Donhowe, J., El-Guebaly, L., Emmert, G., Hopkins, G., Houlberg, W., Johnson, A., Kamperschroer, J., Klein, D., Kulcinski, G., Lott, R., Mcalees, D., Maynard, C., Mense, A., & Neil, G. (1973). UWMAK-I -A Wisconsin Toroidal Fusion Reactor Design.

[13] Rubel, M. (2018). Fusion Neutrons: Tritium Breeding and Impact on Wall Materials and Components of Diagnostic Systems. Journal of Fusion Energy, 38(3-4), 315–329. https://doi.org/10.1007/s10894-018-0182-1

[14] Pena-Pereira, F., & de la Calle, I. (2019, January 1). Solvents and Eutectic Solvents (P. Worsfold, C. Poole, A. Townshend, & M. Miró, Eds.). ScienceDirect; Academic Press.

[15] Bismuth. (n.d.). Nature.berkeley.edu. https://nature.berkeley.edu/classes/eps2/wisc/bismuth.html: :te

[16] Royal Society of Chemistry. (2011). Tin - Element information, properties and uses | Periodic Table. Rsc.org. https://www.rsc.org/periodic-table/element/50/tin

[17] Weber, D. P. (2024, January 10). Characterization of Liquid Metal Free Surface Response to an Electromagnetic Impulse and Implications for Future Nuclear Fusion Devices. Vt.edu; Virginia Tech. https://vtechworks.lib.vt.edu/items/94744f98-f5e3-4f8f-8235-49f526543035

[18] Zuiderveld, Karel. "Contrast Limited Adaptive Histograph Equalization." Graphic Gems IV. San Diego: Academic Press Professional, 1994. 474–485

[19] Ludwig, J. (n.d.). Image Convolution. https://web.pdx.edu/ jduh/courses/Archive/geog481w07/Stude ImageConvolution.pdf

[20] Russ, J. C. (2002). The Image Processing Handbook, Fourth Edition. CRC Press.

[21] Lim, Jae S., Two-Dimensional Signal and Image Processing, Englewood Cliffs, NJ, Prentice Hall, 1990, pp. 469-476

[22] Whitaker, R. T. (2000). A level-set approach to image blending. IEEE Transactions on Image Processing, 9, 11. https://doi.org/10.1109/83.877208

[23] Getreuer, P. (2011). Linear Methods for Image Interpolation. Image Processing on Line, 1(1), 238–259. https://doi.org/10.5201/ipol.2011.g-lmii

[24] Mathur, N., Mathur, S., & Mathur, D. (2016). A Novel Approach to Improve Sobel Edge Detector. Procedia Computer Science, 93, 431–438. https://doi.org/10.1016/j.procs.2016.07.230

[25] Gao, W., Zhang, X., Yang, L., & Liu, H. (2010). An improved Sobel edge detection. IEEE, 5, 67–71. https://doi.org/10.1109/ICCSIT.2010.5563693

[26] Physics 116A The argument of a complex number. (2011). University of California, Santa Clara. https://scipp.ucsc.edu/ haber/ph116A/arg-11.pdf

[27] Shapiro, L. G., Yung, K. T., & Rosenfeld, A. (1996). Connected Component Labeling and Adjacency Graph Construction. In Topological Algorithms for Digital Image Processing (Vol. 19, pp. 1–30). NorthHolland. https://doi.org/10.1016/S09230459(96)800115

[28] Lumia, R., Shapiro, L., & Zuniga, O. (1983). A new connected components algorithm for virtual memory computers. Computer Vision, Graphics, and Image Processing, 22(2), 287–300. https://doi.org/10.1016/0734189X(83)900713

[29] Rosenfeld, A., & Kak, Avinash C. (2014). Digital picture processing: Volume 1 (2nd ed.). Morgan Kaufmann Publishers Inc.

[30] Xu, W., Li, Q., Feng, H., Xu, Z., & Chen, Y. (2013). A novel star image thresholding method for effective segmentation and centroid statistics. Optik, 124(20), 4673–4677. https://doi.org/10.1016/j.ijleo.2013.01.067

[31] Venkateswarlu, R., Sujata, K. V., & B. Venkateswara Rao. (1992). Centroid tracker and aimpoint selection. Proc.SPIE, 1697, 520–529. https://doi.org/10.1117/12.138205

[32] Marques, O. (2011). Practical image and video processing using MATLAB. J. Wiley & Sons/Ieee Press.

[33] Davis, M., & Peebles, E. (1983). A survey of galaxy redshifts. V - The two-point position and velocity correlations. Astrophysical Journal, 267, 465–465. https://doi.org/10.1086/160884

[34] Biadgie, Y., & Sohn, K.-A. (2014). Feature detector using adaptive accelerated segment test. 1–4. https://doi.org/10.1109/ICISA.2014.6847403

[35] Edward Rosten and Tom Drummond. Machine learning for high-speed corner detection. SpringerLink, 1970

[36] BarShalom, Y., & Tse, E. (1975). Tracking in a cluttered environment with probabilistic data association. Automatica, 11(5), 451–460. https://doi.org/10.1016/00051098(75)900217

[37] Kirubarajan, T., Wang, H., Bar-Shalom, Y., & Pattipati, K. R. (2001). Efficient multisensor fusion using multidimensional data association. IEEE Transactions on Aerospace and Electronic Systems, 37, 2. https://doi.org/10.1109/7.937457

[38] Zhu, A. Z., Atanasov, N., & Daniilidis, K. (2017). Event-based feature tracking with probabilistic data association. 4465–4470. https://doi.org/10.1109/ICRA.2017.7989517

[39] Rasmussen, C., & Hager, G. D. (2001). Probabilistic data association methods for tracking complex visual objects. IEEE Transactions on Pattern Analysis and Machine Intelligence, 23, 6. https://doi.org/10.1109/34.927458

[40] Rakai, L., Song, H., Sun, S., Zhang, W., & Yang, Y. (2022). Data association in multiple object tracking: A survey of recent techniques. Expert Systems with Applications, 192, 116300. https://doi.org/10.1016/j.eswa.2021.116300

[41] Ballantine, J. P., & Jerbert, A. R. (1952). Distance from a Line, or Plane, to a Poin. The American Mathematical Monthly, 59(4), 242–243. https://doi.org/10.2307/2306514

[42] Ward, D. (1995). ROGOWSKI COILS. Rocoil Limited.

[43] Weerawoot Kanokbannakorn, Komsan Hongesombut, Nithiphat Teerakawanich, & Siwapon Srisonphan. (2016). Arc flash hazard in distribution system with distributed generation. Procedia Computer Science, 86, 377–380. https://doi.org/10.1016/j.procs.2016.05.106

[44] Nogi, K., Ogino, K., McLean, A., & Miller, W. A. (1986). The temperature coefficient of

the surface tension of pure liquid metals. Metallurgical Transactions B, 17(1), 163–170. https://doi.org/10.1007/bf02670829

[45] Dickey, M. D. (2021). Liquid metals at room temperature. Physics Today, 74(4), 30–36. https://doi.org/10.1063/pt.3.4723

[46] FASTCAM MINI AX. (2017). Photron. https://photron.com/fastcam-mini-ax/

[47] Rio, del, Gautam, G. S., & Carter, E. A. (2020). Deuterium addition to liquid Li–Sn alloys: implications for plasmafacing applications. Nuclear Fusion, 60(1), 016025. https://doi.org/10.1088/17414326/ab523c

[48] Dobosz, A., & Gancarz, T. (2018). Reference Data for the Density, Viscosity, and Surface Tension of Liquid Al–Zn, Ag–Sn, Bi–Sn, Cu–Sn, and Sn–Zn Eutectic Alloys. Journal of Physical and Chemical Reference Data, 47(1), 013102. https://doi.org/10.1063/1.5010151

[49] Ongena,J.(2016).Nuclear fusion and its large potential for the future world energy supply. Nukleonika,61(4) 425-432. https://doi.org/10.1515/nuka-2016-0070

[50] Heat Sheets, Adhesive Ready, Circular, 10W/sq. in., 6” Overall Diameter. (2019). Mcmaster-Carr. https://www.mcmaster.com/35765K93/

[51] Heat Sheets, Adhesive Ready, 10W/sq. in., 24” Long x 1” Wide Overall. (2019). McMaster-Carr. https://www.mcmaster.com/35765K71/

[52] Heat Sheets, Adhesive Ready, 10W/sq. in., 24” Long x 1” Wide Overall. (2019). McMaster-Carr. https://www.mcmaster.com/35765K71/

[53] Heat Sheets, Adhesive Ready, 2.5W/sq. in., 12” Long x 6” Wide Overall. (2019). McMaster-Carr. https://www.mcmaster.com/35765K251/

[54] Wood, J., Jawad, B., and Riedel, C., ”Effect of Temperature on Weld Strength in Chrome Moly Space Frames,” SAE Technical Paper 2006-01-3648, 2006

[55] Tkachuk, M. A., Golovin, S. V., Éfron, L. I., & Ganoshenko, I. V. (2020). Effect of Alloying With Molybdenum and Chromium on Low-Carbon Pipe Steel Structure and Properties. Metallurgist, 63(9-10), 1043–1053. https://doi.org/10.1007/s11015-020-00923-y

[56] Chromalox A-65 120 Volt 660 Watt Ring Heater 3 PACK. (2024, February 24). Thermal Devices. https://www.thermaldevices.com/product/chromalox-a-65-120-volt-660-watt-ring-heater/

[57] Ring Heaters | Chromalox. (2024). Chromalox.com. https://www.chromalox.com/en/products-and-technologies/component-technologies/strip-and-ring-heaters/ring-and-disc-heaters/ring-heaters

[58] Santarius, J. F. (1992). Magnetic Fusion for Space Propulsion. Fusion Technology, 21(3P2B), 1794–1801. https://doi.org/10.13182/fst92-a29980

[59] About Plasmas and Fusion. (n.d.). Princeton Plasma Physics Laboratory.

[60] Meier, W. R. (2014). Tritium Breeding Blanket for a Commercial Fusion Power Plant - A System Engineering Assessment. Office of Science and Technology, US Department of Energy. https://doi.org/10.2172/1305833

[61] Liu, C., Li, Y., Lin, D., Hsu, P.-C., Liu, B., Yan, G., Wu, T., Cui, Y., & Chu, S. (2020). Lithium Extraction from Seawater through Pulsed Electrochemical Intercalation. Joule, 4(7), 1459–1469. https://doi.org/10.1016/j.joule.2020.05.017

[62] Barbosa, H., Soares, A. M. V. M., Pereira, E., & Freitas, R. (2023). Lithium: A review on concentrations and impacts in marine and coastal systems. Science of the Total Environment, 857, 159374. https://doi.org/10.1016/j.scitotenv.2022.159374

[63] W. Mueller, R. (2017). Navigating Hong Kong's return to China. American Foreign Service Association; The Foreign Service Journal.

[64] Fusion in brief. (n.d.). Culham Centre for Fusion Energy; UK Atomic Energy Authority.

[65] Sethian, J.D., Robson, A.E. The dense Z-pinch: An alternative approach to fusion. J Fusion Energ 10, 329–330 (1991). https://doi.org/10.1007/BF01052135

[66] DERZON, MARK S, ROCHAU, GARY E, DEGROOT, J, OLSON, CRAIG L, PETERSON, P, PETERSON, R R, SLUTZ, STEPHEN A, & ZAMORA, ANTONIO J. An Inertial-Fusion Z-Pinch Power Plant Concept. United States.

[67] Stone, Howard A., Koel, Bruce E., Bernasek, Steven L., Carter, Emily A., Debenedetti, Pablo G., & Panagiotopoulos, Athanassios Z. Liquid Metals as Plasma-facing Materials for Fusion Energy Systems: From Atoms to Tokamaks. United States. https://doi.org/10.2172/1389595

[68] Piovesan, P., M, H. J., Martin, P., A, N. G., Turco, F., Bialek, J., M, F. N., La, J, L. M., Okabayashi, M., Paz-Soldan, C., J, S. E., D, T. A., Zanca, P., Baruzzo, M., Bolzonella, T., W, H. A., L, J. G., Marrelli, L., & Piron, L. (2014). Tokamak operation with safety factor q95<2 via control of MHD stability. Phys. Rev. Lett., 113(4), 045003. https://doi.org/10.1103/PhysRevLett.113.045003

[69] U. Shumlak and C.W. Hartman (1995). "Sheared Flow Stabilization of the m=1 Kink Mode in Z-Pinches," Physical Review Letter 75, (18) 3285

[70] U. Shumlak, B.A. Nelson, R.P. Golingo, S.L. Jackson, E.A. Crawford, and D.J. Den Hartog (2003). "Sheared flow stabilization experiments in the ZaP flow Z-pinch," Physics of Plasmas 10, (5) 1683

[71] Chen, Y., Dorris, Z., Gallardo, A., Gupta, A., Hoffman, C., Humphreys, A., Mejia, J., & Wiedman, A. (2024). Digital Repository at the University of Maryland (DRUM). Umd.edu. https://drum.lib.umd.edu/items/7b5622a3-a769-46b3-8ca7-7d05e24e5b8b

[72] J. C. Valenzuela, I. Krasheninnikov, F. Conti, F. Wessel, V. Fadeev, J. Narkis, M. P. Ross, H. U. Rahman, E. Ruskov, F. N. Beg; Injector design for liner-on-target gas-puff experiments. Rev. Sci. Instrum. 1 November 2017; 88 (11): 113509. https://doi.org/10.1063/1.4997429

[73] C. Chen, E. S. Lavine, W. M. Potter, C. E. Seyler, B. R. Kusse; Axial confinement of wire array Z-pinch precursor plasmas by a pulsed magnetic mirror field. Phys. Plasmas 1 July 2024; 31 (7): 072704. https://doi.org/10.1063/5.0207561

[74] Burdiak GC, Lebedev SV, Suzuki-Vidal F, et al. Cylindrical liner Z-pinch experiments for fusion research and high-energy-density physics. Journal of Plasma Physics. 2015;81(3):365810301. doi:10.1017/S0022377815000318

Appendices

Appendix A

MATLAB Codes

1. Code to process images, begin tracking ejecta particles:

```
\small

close all
clear all
clc

location = '/Users/vigneshsridhar/Library/CloudStorage/GoogleDrive-vigneshsridhar@vt.edu
/Shared drives/Adams Plasma Laboratory/Liquid Electrode eXperiment/Testing Data/Imaging/2022062401/*.png';

ds = imageDatastore(location);
num_frames = 100;
centroids_history = cell(1, num_frames);
roi_size = [50, 50];
rois = cell(num_frames, 1);
roi = [322.51, 6.51, 779.98, 1663.98]; %2022062401
resize_factor = 2.5;
crop_rect = [840.51, 477.51, 149.98, 166.98];

% Data storage for edges
edges_data = struct('Frame', [], 'EdgePixels', []);
```

```
all_centroids = [];
all_areas = [];
all_radii = [];
all_circularity = [];

gif_filename = 'finalprezigif2.gif';

for i = 55:100
    img = readimage(ds, i);
    resizeimg = imresize(img, resize_factor);
    cropimg = imcrop(resizeimg, crop_rect);

    grayImage = im2gray(cropimg);
    grayImage = adapthisteq(grayImage); % Adaptive histogram equalization

    gaussianFilter = fspecial('gaussian', [15, 15], 2.0);

mean_image = imfilter(grayImage, gaussianFilter, 'replicate');

     mean_image1 = imfilter(grayImage, fspecial('average', [15, 15]), 'replica
         ');
    subtract = grayImage - mean_image;

    % Adaptive thresholding
    binaryImage1 = imbinarize(subtract, 'adaptive', 'Sensitivity', 0.4);

    % Noise reduction
    binaryImage = medfilt2(binaryImage1, [3, 3]); % Median filtering

    J = binaryImage;
```

```
    K = cropimg;

 I1 = K;

    I2 = J;

    magnificationFactor = 10.0;
    F1 = imresize(I1, magnificationFactor);
    F2 = imresize(I2, magnificationFactor);

    F4 = imresize(I2, magnificationFactor);
%     F9 = edge(F4, 'Canny');

    F5 = imfuse(F1, F4);
    F6 = im2gray(F5);
    F7 = imfuse(F1, F4);
    F1_roi = imcrop(F1, roi);
    F2_roi = imcrop(F2, roi);
    F5_roi = imcrop(F5, roi);
    F6_roi = imcrop(F6, roi);
%     F9_roi = imcrop(F9, roi);
    F10_roi = edge(F6_roi);

    % Blob detection using connected components
    cc = bwconncomp(F10_roi);
    stats = regionprops(cc, 'Area', 'PixelIdxList', 'Centroid', 'EquivDiameter',
    'Circularity');

    all_areas = [all_areas; [stats.Area]'];  % Collect areas
    all_radii = [all_radii; [stats.EquivDiameter]' / 2];
```

```
    all_circularity = [all_circularity; [stats.EquivDiameter]'];

    % Extract pixel indices of edges
    edge_pixels = [];
    for j = 1:length(stats)
        edge_pixels = [edge_pixels; stats(j).PixelIdxList];
    end

    % Convert linear indices to subscripts (x, y coordinates)
    [rows, cols] = ind2sub(size(F10_roi), edge_pixels);
    edge_positions1 = [cols, rows]; % Adjusting to original image coordinates
    edge_positions = [cols + roi(1), rows + roi(2)];

    % Adjust coordinates for resized image
    edge_positions(:, 1) = edge_positions(:, 1) / magnificationFactor;
    edge_positions(:, 2) = edge_positions(:, 2) / magnificationFactor;

    % Adjust coordinates for original image
    edge_positions(:, 1) = edge_positions(:, 1) + crop_rect(1);
    edge_positions(:, 2) = edge_positions(:, 2) + crop_rect(2);
    edge_positions = edge_positions / resize_factor;

     centroids2 = cat(1, stats.Centroid);

    centroids = cat(1, stats.Centroid);
    centroids(:, 1) = centroids(:, 1) + roi(1);
    centroids(:, 2) = centroids(:, 2) + roi(2);
    centroids = centroids / magnificationFactor;
    centroids(:, 1) = centroids(:, 1) + crop_rect(1);
    centroids(:, 2) = centroids(:, 2) + crop_rect(2);
    centroids = centroids / resize_factor;
```

```

    centroids_history{i} = [centroids, repmat(i, size(centroids, 1), 1)];

        all_centroids = [all_centroids; centroids_history{i}];

   Visualize the edges on the original image
    imshow(img); hold on;
    plot(edge_positions(:, 1), edge_positions(:, 2), 'g.');
    plot(centroids(:, 1), centroids(:, 2), 'r*');
    hold off;
    pause(0.5);
```

2. Code to sift through calculated position points

```
\small

clear all
close all
clc

data = readtable('/Users/vigneshsridhar/Desktop/Ejecta Tracking
Codes/2023030201codes/2023030201trial081224.xlsx');

data.Properties.VariableNames = {'x', 'y', 'frame_number'};

particles = {};

% Parameters
distance_threshold = 3;  % Maximum distance to consider points as the same
    particle
max_frame_gap = 1;         % Maximum number of frames to allow a gap in
    particle tracking
```

```
17
18 particle_id = 0;
19
20 upward_movement_threshold = 5;
21
22 frames = unique(data.frame_number);
23
24 for i = 1:length(frames)
25     frame = frames(i);
26     current_frame_data = data(data.frame_number == frame, :);
27
28     for j = 1:height(current_frame_data)
29         x = current_frame_data.x(j);
30         y = current_frame_data.y(j);
31
32         % Find the nearest existing particle
33         min_distance = inf;
34         nearest_particle = [];
35
36         for k = 1:length(particles)
37             last_position = particles{k}(end, :);
38
39             % Check if the particle already has a point for this frame
40             if any(particles{k}(:, 3) == frame)
41                 continue;
42             end
43
44             % Check if the particle is within the maximum frame gap
45             if frame - last_position(3) > max_frame_gap
46                 continue;
47             end
```

```

            distance = sqrt((last_position(1) - x)^2 + (last_position(2) - y)^2);

            if distance < min_distance && distance < distance_threshold
                min_distance = distance;
                nearest_particle = k;
            end
        end

        if ~isempty(nearest_particle)
            particles{nearest_particle}(end + 1, :) = [x, y, frame];
        else
            % Create a new particle
            particle_id = particle_id + 1;
            particles{particle_id} = [x, y, frame];
        end
    end
end

% Convert the particle data into a table, filtering out particles that
particle_data = [];

for k = 1:length(particles)
    positions = particles{k};

    % Calculate the total distance traveled
    total_distance = 0;
    for m = 2:size(positions, 1)
        total_distance = total_distance + sqrt((positions(m, 1) - positions(m-1, 1))^2 +
```

```
        (positions(m, 2) - positions(m-1, 2))^2);

    end

    % Check if the particle moves upward significantly
    initial_y = positions(1, 2);
    final_y = positions(end, 2);
    upward_movement = initial_y - final_y;

    % Check if the particle starts tracking within the specified frame range,
    % has moved at least a distance of 20, and moved upward significantly

      if upward_movement >= upward_movement_threshold && size(positions, 1) >=
          8

        pid = k;

        for m = 1:size(positions, 1)
            x = positions(m, 1);
            y = positions(m, 2);
            frame = positions(m, 3);
            particle_data = [particle_data; pid, x, y, frame];
        end
    end
end

particle_table = array2table(particle_data, 'VariableNames', {'particle_id', '
    x', 'y',
'frame_number'});
```